RADIATION MODELLING OF VACUUM FIELD EMISSION DEVICES

By

Adam Fisher Reynolds, First Lieutenant, U.S. Army

B.S., Nuclear Engineering (2017) United States Military Academy

SUBMITTED TO THE
DEPARTMENT OF NUCLEAR SCIENCE AND ENGINEERING

IN PARTIAL FULFILLMENT OF THE REQUIREMENTS FOR THE DEGREE OF
MASTER OF SCIENCE IN NUCLEAR SCIENCE AND ENGINEERING

AT THE
MASSACHUSETTS INSTITUTE OF TECHNOLOGY
JUNE 2019

Signature of Author: _____
Adam Fisher Reynolds, First Lieutenant, U.S. Army
Department of Nuclear Science and Engineering
April 28, 2019

Certified by: _____
Benoit Forget
Associate Professor of Nuclear Science and Engineering
Thesis Supervisor

Certified by: _____
Peter Miraglia, PhD.
Distinguished Member of Technical Staff, Draper
Draper Fellow Advisor and Thesis Reader

Accepted by: _____
Ju Li
Battelle Energy Alliance Professor of Nuclear Science and Engineering
and Professor of Materials Science and Engineering
Chair, Department Committee on Graduate Students

Radiation Modelling of Vacuum Field Emission Devices

by

Adam Fisher Reynolds, First Lieutenant, U.S. Army

Submitted to the Department of Nuclear Science and Engineering
on April 28, 2019, in Partial Fulfillment of the Requirements for
the Degree of Master of Science in Nuclear Science and Engineering

ABSTRACT

Recent advances in micro and nanofabrication techniques have enabled modern vacuum field emission devices (VacFEDs) and have been demonstrated in the laboratory for use as diodes and transistors. Modern VacFEDs operate through cold emission of electrons across a vacuum gap. It has been proposed that these devices are "radiation insensitive" since they do not have a solid-state junction as in other modern electronic devices. Radiation testing has been conducted to characterize the radiation response for these devices however, minimal supporting modeling has been performed. This thesis attempts to model and quantify the radiation effects of modern VacFEDs. It focuses primarily on two effects associated with ionizing radiation exposure to a VacFED diode materials and structure: 1) The production of a net electron Direct Drive (DD) current in conductive layers due to imbalance in ionization rates in device layers and 2) Radiation Induced Conductivity (RIC) due to creation and drift of electron-hole pairs across an electric field of a dielectric insulating layer. These currents are treated as a noise sources that compete with the output signal of the device. Two radiation transport codes are used quantify interaction, electron charge and energy deposition of consequence to direct drive and RIC effects: 1) CEPXS/ONEDANT: a 1-dimensional electron-photon discrete ordinates code package and 2) MCNP6: a general-purpose, continuous-energy, generalized-geometry, time dependent, Monte Carlo radiation-transport code. RIC response was found to have the greatest current for all device models considered over all energies. This thesis found a dose rate of 6×10^6 rad(Si)/s at the surface of a VacFED diode is required to cause a 0.1 μA noise current in a device designed to operate at 1.0 μA. This finding suggests that VacFED technology has the capability to operate continuously in a modern pressurized water nuclear reactor core gamma ray environment, which has an approximate dose rate of 3×10^5 rad(Si)/s.

Thesis Supervisor: Benoit Forget
Title: Associate Professor of Nuclear Science and Engineering

Acknowledgements

I owe thanks to many people for allowing me to successfully complete this thesis and graduate from such a great institution. I would like to take the time to specifically thank the following:

- Draper: thank-you for sponsoring my research and studies as a member of the Draper Fellow Program. This has given me a truly amazing opportunity before my Army career begins.
- Peter Miraglia, PhD.: thanks for the countless hours you have spent mentoring me in my research. There were many times you could have given me a simple answer and made things easier on yourself, but instead you took the time to truly teach me and make sure I understood the concepts behind my research.
- Dr. Benoit Forget: thanks for guiding my thesis as an advisor. Your questions during our meetings exposed gaps in my understanding and led to the development of a much stronger thesis.
- The U.S. Army: thanks for giving soldiers, such as me, the ability to further their education. I hope to someday use the lessons I learned here to better serve my country, which has given me the opportunity to be here and live a fulfilling life.
- West Point, the Department of Physics and Nuclear Engineering: thanks for adequately preparing me to take on a degree in Nuclear Engineering at MIT.
- Nina: your support as the most amazing wife in the world made this process so much easier. You inspire me every day.
- Mom and Dad: thanks Mom and Dad for supporting me my entire life. You allowed me to pursue my dreams and gave me practically free rein as a child to explore what excites me.
- George and Alice: thank-you for your support as the best in-laws in the world. I am truly grateful and proud to be a new member of your family.
- My friends here at MIT: I have made some of the best friends here in such a short amount of time. You are always there to help me when I need it and I am truly grateful. Thanks for keeping me sane. I will forever miss our ritual Tuesday night trivia. Special thanks to Isaac, Lucas, Sterling, Guillaume, Brian, Abhi, Mohammad, and Kieran for being a part of my wedding.

Contents

1 Introduction

The recent development of vacuum field emission devices (VacFEDs) allows for the creation of diodes and transistors without the use of a solid-state semiconductor. These modern VacFEDs operate through cold field emission of electrons and thus do not have the same thermal wearout issues of previous vacuum tubes. Radiation effects in modern electronic systems primarily occur at the solid p-n junction of the semiconductor or at the gate-oxide of a transistor. VacFEDs have neither of these vulnerable features and thus offer unique radiation-resistant properties. Therefore, VacFEDs offer superior performance for application in high radiation environments, such as space, nuclear reactors, and in medical physics applications. This introduction will give a brief overview of radiation effects on conventional electronics. Modern VacFEDs will be introduced as a potential solution to the problems associated with operating electronics in high ionizing radiation environments. The objective of this thesis is to predict and quantify the tolerance of a modern VacFED for radiation effects that are of concern to their continuous operation in the high dose rate environment of a nuclear reactor.

1.1 Radiation Effects on Conventional Electronics

There are a plurality of different modalities that cause radiation effects and failure in conventional electronics. The following subsections provide a brief introduction of three major effects.

1.1.1 Total Ionizing Dose Effects

Total Ionizing Dose (TID) effects are caused by cumulative ionization in electronic materials. Insulators are particularly susceptible to TID effects, where ionizations create electron-hole pairs and the holes are subject to trapping. Metal Oxide Semiconductor (MOS) devices are the most common devices used for modern transistors. They operate through use of a gate insulated by an oxide, as shown in Figure 1. Gate-bias refers to the voltage applied to the device to manipulate drain current. In MOS devices, ionizing radiation causes positive charges to be trapped near the Si/SiO_2 interface. This causes gate threshold voltage shifts that affect device performance [1]. A large enough threshold shift will move the operating point of the device and ultimately result in functional failure (where the device either remains in the open or closed state). Figure 2 shows the impact of radiation on the Drain-Source Current of a nMOS transistor. A nMOS transistor is a MOS device that turns on with positive gate bias. TID causes

threshold that will drift negatively with increasing exposure. Figure 1 illustrates that exposure to 1 Mrad (SiO_2) of ionizing radiation clearly shifts the operating voltage- gate bias-to a more negative value, requiring lower voltage to turn on the device.

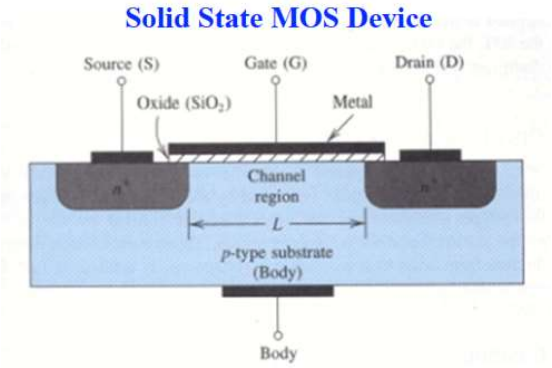

Figure 1- Basic MOS device.

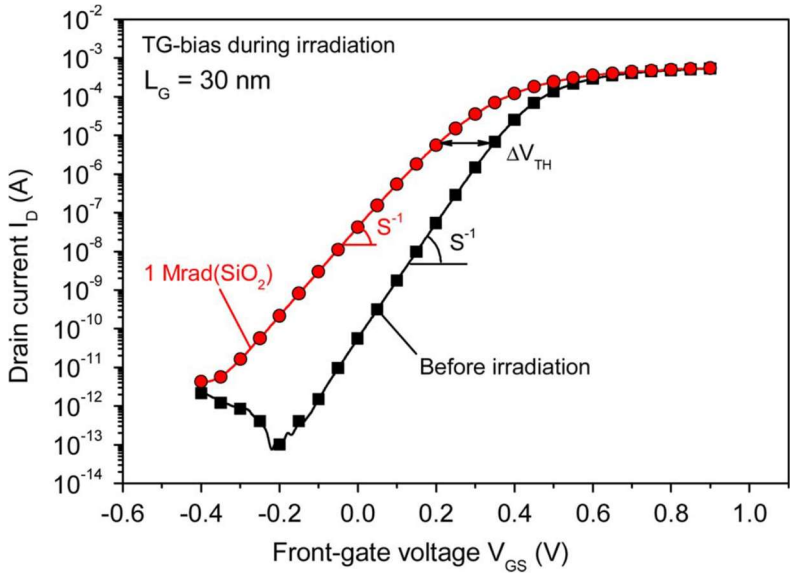

Figure 2- Drain current, I_D, vs front gate voltage at V_{DS} = 0.1 V of a typical nMos transistor from [1].

1.1.2 High Dose Rate Responses and Single Event Effects (SEEs)

High dose rates can also cause instantaneous, transient effects in the operation of electronics if the exposure occurs in a short pulse. In space environments, the concern is often the transient ionization in

a single transistor of a microcircuit by protons or heavy ions, referred to as Single Event Effects (SEEs). SEEs are commonly classified by their Linear Energy Transfer (LET), which is the energy that an ionizing particle transfers to the material traversed per unit distance. Particles with LET (less than 30 MeV*cm^2/mg) commonly create SEEs that cause changes in the digital state of a digital node. This results in logic and memory-related issues. In less common collisions, high LET (greater than 30 MeV*cm^2/mg) particles create enough ionization to open parasitic conduction paths that burn out due to excessive current draw in heating [2]. SEEs are statistically random and the effects are a function of the probability and consequence of certain interactions.

In nuclear reactors, the dose rates are much greater than the background radiation rates in a typical space mission and impinge upon the entire device in a continuous steady state stream. Ionizing radiation deposited at high rates in the semiconductors used in modern microelectronics leads to the creation of electron-hole pairs in the junction of the depletion region, as shown in Figure 3. The number of electron-hole pairs is equal to the energy of the dose deposited in the depletion region divided by the energy to create an electron-hole pair (3.6 $\frac{eV}{eh\ pair}$ for silicon). The high dose rates experienced in nuclear reactors can create radiation-induced currents that generate noise and if high enough, could ultimately cause device failure through joule heating.

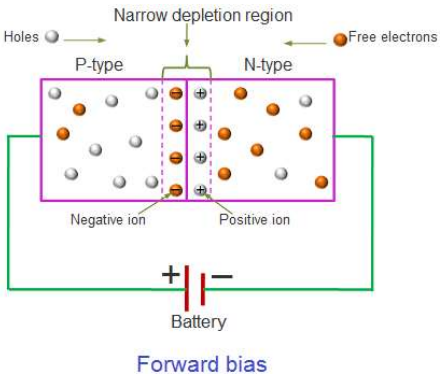

Figure 3- Semiconductor Diode in Forward Bias from [3].

1.1.3 Neutron Displacement Damage

Neutrons create damage to crystalline semiconductors by knocking atoms out of their intended positions and producing material defects in the lattice. These displacement effects degrade the operation of conventional electronics in high neutron flux environments, such as nuclear reactors. In bipolar transistors, displacement damage reduces minority carrier lifetime and saturation voltage due to gain degradation and increased silicon resistivity. Minority carriers, the less abundant charge carriers in a semiconductor, are either electrons or holes, depending on the doping of the semiconductor. Figure 4 provides an example of neutrons increasing the operation voltage of a bipolar transistor [4].

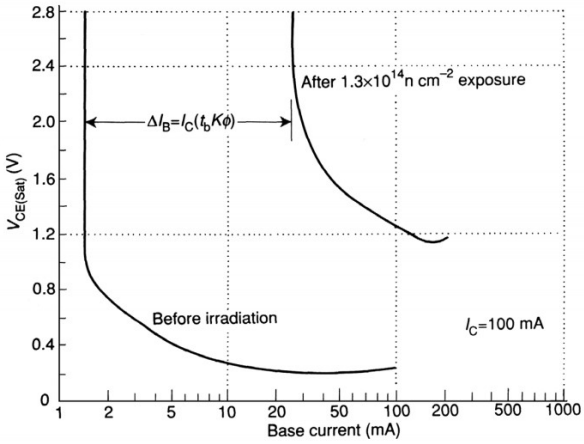

Figure 4- Increase of the saturation voltage of 2N1613 bipolar transistor, irradiated from a neutron-gamma source up to dose 1.3x10^{14} n-cm^{-2} from [4].

1.2 The Modern VacFED

Recent advances in micro and nanofabrication techniques have enabled the development of modern vacuum field emission devices (VacFEDs). They have been demonstrated in the laboratory for use as diodes and transistors [5]. These VacFEDs do not have a solid junction between the anode and cathode, but rather a vacuum gap. This vacuum gap has virtually no material to respond to radiation offers a purported radiation insensitivity because it replaces the solid-state junction found in modern diodes and transistors [6] [5].

The “lateral” design of the modern VacFEDs explored in this thesis were pioneered at Vanderbilt University [5]. VacFEDs are created using a single mask process to create a layered structure shown below in Figure 5. This structure is created by first starting with a thick Si substrate layer, a thin layer of SiO_2, and a thin poly-Si layer. Plasma enhanced chemical vapor deposition (PECVD) is used to grow a thin layer of nanodiamond as the conducting and emission layer of the cathode and anode. Finally, Reactive Ion Etching and Si etching are used to produce the desired shape of the device. The thickness of the substrate is on the order of hundreds of microns and the thicknesses of the other layers are usually less than a few microns. All devices are configured with structured tips similar to those shown in Figure 6 (left). The sharp tips of these fingers allow electrons to be emitted from the cathode to the anode under an applied voltage above the field emission threshold. A finite current density can travel through each tip while maintaining tip integrity. VacFEDs have been designed to operate as both diodes and transistors, which enables a potential wider range of future applications for these devices. Figure 6 shows the basic design of VacFEDs in the diode and transistor configurations [7]. The image on the left shows the VacFED in a diode configuration with multiple cathode tips. The image on the right shows the VacFED in a triode configuration, which function as a transistor with a voltage applied at the gate influencing the current across the cathode-anode gap.

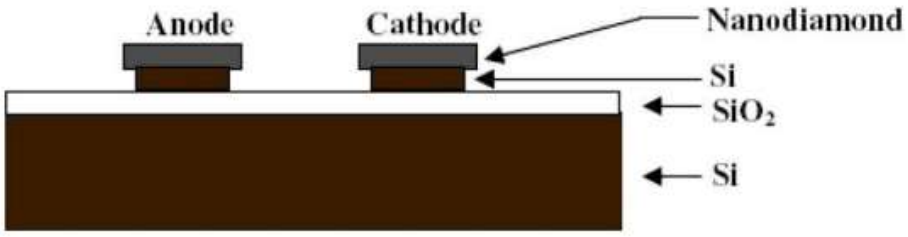

Figure 5- Basic structure of VacFED after fabrication from [7].

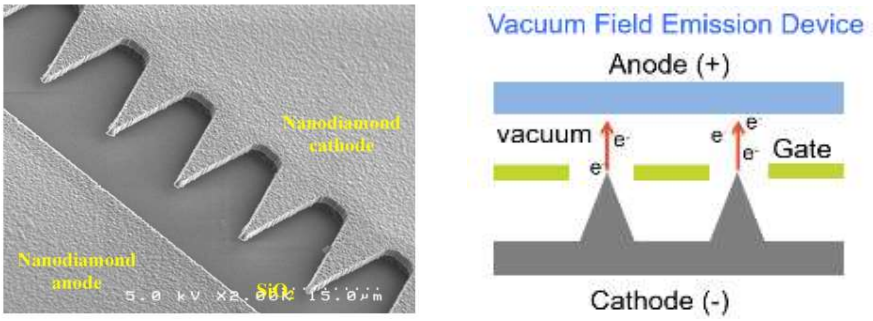

Figure 6- VacFED in diode configuration with multiple cathode tips (left) from [7]. VacFED in triode configuration (right). The triode functions as a transistor with a voltage applied at the gate influencing current across the cathode-anode gap.

Previous testing has demonstrated the theorized "radiation-insensitivity" of VacFEDs. In one experiment, a "125 finger" (consisting of 125 cathodes on a single anode) VacFED diode was exposed to a 15 Mrad total ionizing 10keV x-ray dose with at a dose rate of 31.5 krad(SiO_2)/min [5]. No change within measurement error was observed in the I-V response curve of the diode before and after radiation. Neutron exposure was also carried out by exposing the diodes to 4.4 x 10^{13} neutrons/cm^2 with 5.6 x 10^{12} of these neutrons having an energy greater than 3 MeV [7]. These experiments found no changes to resistivity, dilation, emission, or changes to the I-V response, within measurement error, after neutron exposure. This test device was also exposed to a temperature of 200 degrees Celsius and no response effects were observed. The response functions before and after exposure to high total dose, neutron fluence, and temperature are plotted in Figure 7 [8] [7].

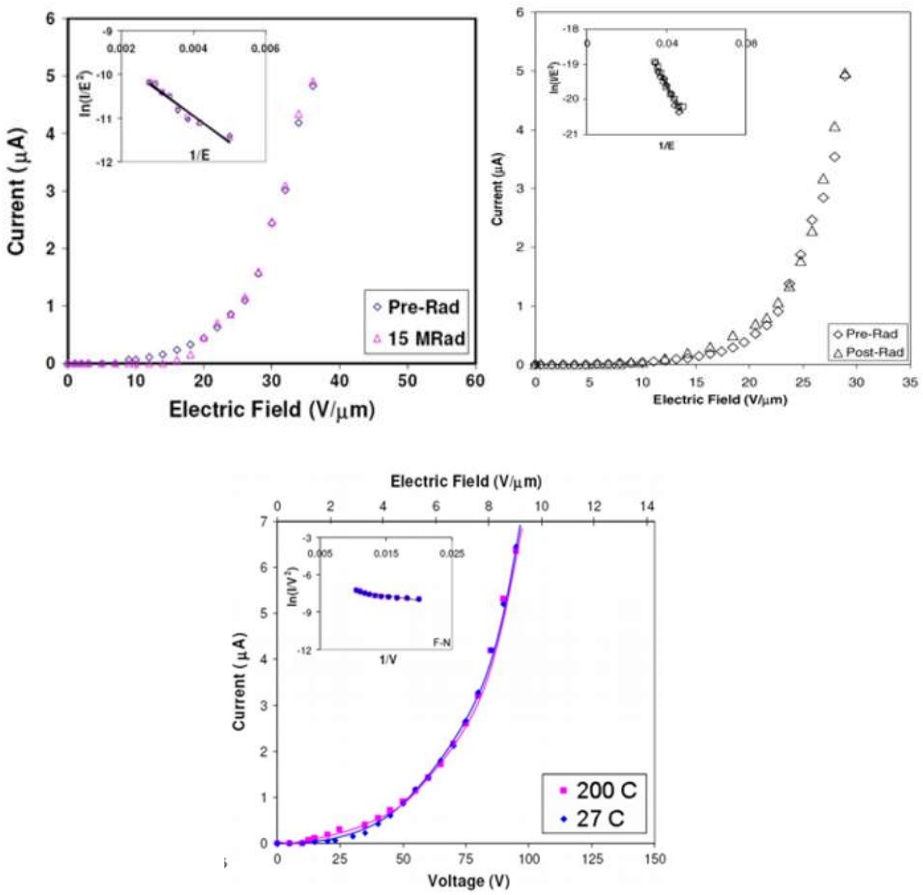

Figure 7- Current response functions of VacFED diode due to 15 Mrad X-ray dose, 4.4 x 10^{13} n/cm^2 fluence, and 200 ℃ respectively [7] [8].

These previous experiments show that VacFEDs outperform current solid-state devices after exposure to ionizing radiation and neutron displacement damage. The effects on these devices were measured before and after they were exposed to radiation, as is standard for conventional semiconductor electronics. No discernable effects were found, suggesting VacFEDs can endure high levels of radiation with no permanent effects. Testing during operation, referred to as “live testing” was not conducted. Live performance must be considered for practical application of any device in a nuclear reactor environment. This thesis will model and quantify the live effects of radiation and propose operational tolerance limits for modern devices.

The diagram introduced in Figure 8 provides a rough sketch of the range of temperatures and total ionizing dose at which different device technologies can operate. The oval representing VacFEDs is largely speculative due to the lack of previous radiation research.

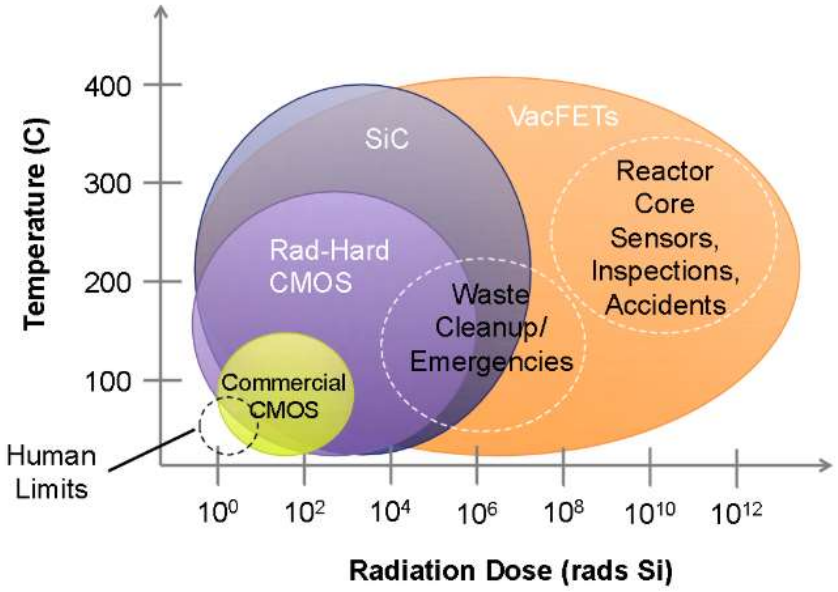

Figure 8- Diagram roughly outlining operational capabilities of different transistor device technologies as a function of total dose and temperature.

2 Theory and Analytical Model

This section provides an introduction and the theory behind two effects from persistent ionizing gamma-ray radiation exposure. These effects have the potential to impact performance of VacFEDs in a nuclear reactor environment. The first, Direct Drive (DD) current, is an electrical current that arises as a result of imbalances in electron production and absorption in the different material layers of the VacFEDs. The second, Radiation Induced Conductivity (RIC), results from dose-rate induced conductivity of insulating material and leakage current from ground layers to the anode through an insulating layer under bias. These currents create noise sources that compete with the output signal of the devices.

2.1 Direct Drive Current

Direct drive current is a net electrical current in a layer that arises as a result of imbalances in electron production and deposition in the different materials of the VacFEDs. Direct drive current results in a net electron charge deposition in a conducting layer or for a time dependent source, or a net electron current. Electrons are produced in gamma interactions with materials in proportion to their interaction cross section. Figure 9 and Equation (1) show how direct drive charge deposition or current can be estimated analytically in a simplified 1-dimensional case for an arbitrary slab of material,

$$i_{DD} = \sum i_{in} - \sum i_{out} = i_{in1} + i_{in2} - i_{out1} - i_{out2} \quad (1)$$

where i_{DD} is the direct drive current, i_{in} (green arrows) represents an incoming current of electrons to the slab, i_{out} (red arrows) represents an outgoing current.

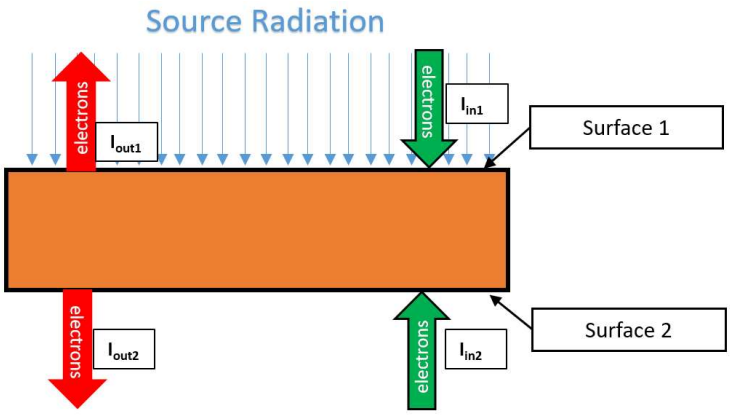

Figure 9- Diagram of 1-dimensional model of electron current in a slab of a single material.

A net imbalance of electrons entering and exiting a given slab of material is a function of the probability of production of free electrons and the probability of stopping these free electrons in the layer. The following sections will underline the primary processes for electron production and transport.

2.1.1 Production of Electrons by Photons

High energy photon interactions with matter create ionizations and free electrons in a radiation environment. The probability of interaction or cross section is a material property and is represented by the linear attenuation coefficient, μ, which describes the fraction of a beam of x-rays or gamma rays that is absorbed or scattered per unit thickness of the absorber material. The change in intensity of a gamma or x-ray beam is described by Equation (2). This equation is used to calculate the number of gamma rays that reach a certain distance through a material without interacting with the electrons in the material,

$$I = I_0 e^{-\mu x} \tag{2}$$

where I is the beam intensity, I_0 is the initial beam intensity, μ is the attenuation coefficient, and x is the thickness of material. Figure 10 shows the attenuation coefficient divided by the density, μ/ρ for Silicon and Carbon (graphite) over a range of energies.

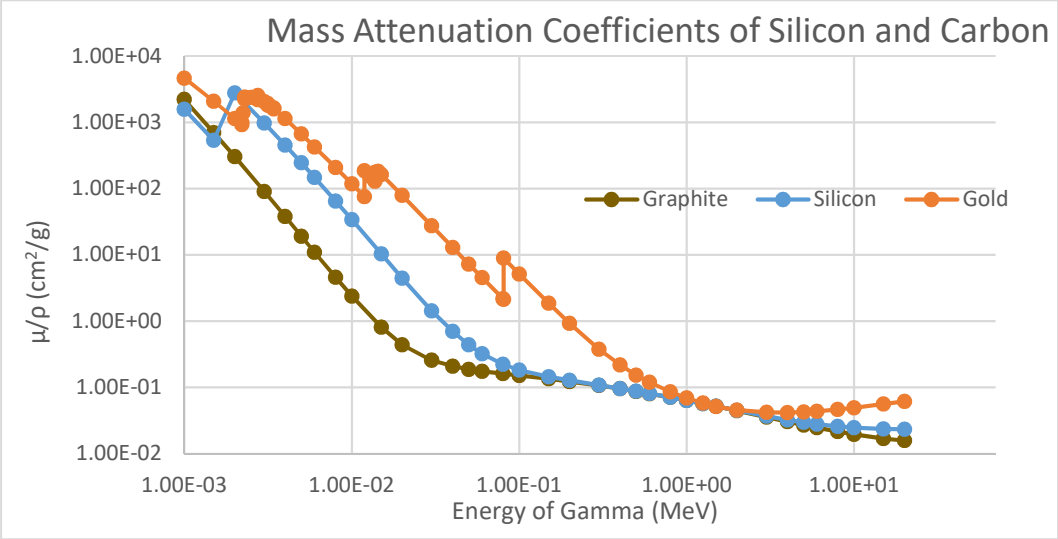

Figure 10- Mass attenuation coefficients (μ/ρ) plotted vs. energy of incident photon for silicon and carbon (graphite) from [9].

Photons can interact with matter in one of three ways: photoelectric effect, Compton scattering, and pair-production. All three of these create ionizations. In the photoelectric effect, a free electron is emitted with energy relatively equal to the energy of the incident gamma ray. In Compton scattering, recoil electrons are freed with a spectrum of energies based on factors such as the incoming gamma energy, mass of target nucleus, and angle of scattered particle. In pair-production, an electron-positron pair is emitted in opposite directions. The likelihood of one mechanism occurring over the other is a function of the atomic number and energy of the incident gamma as shown in Figures 10 and 11. Photoelectric effect is dominant over high atomic number and low photon energy. Compton is the most common over commonly encountered gamma ray energies and is dominant for most engineering materials of low atomic number. Pair-production only occurs at high-energies and is increasingly common as atomic number increases. The following section briefly describes each process.

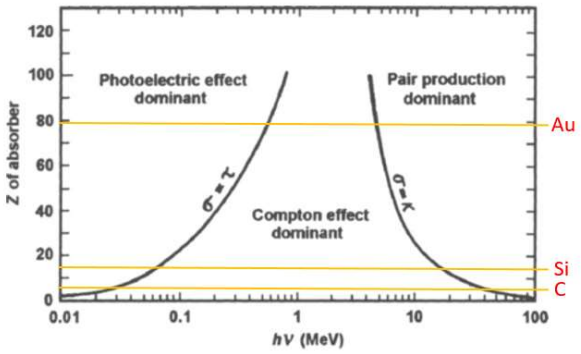

Figure 11- Regions of Dominance for Photon Interactions with Matter from [10].

2.1.1.1 Photoelectric effect

In the photoelectric absorption process, a photon undergoes an interaction with an absorber atom in which the photon completely disappears. In its place, an energetic photoelectron is ejected from one of the bound shells of the atom. The energy of an electron liberated from the photoelectric effect is shown in Equation (3),

$$E_k = hf - \varphi \tag{3}$$

where E_k is the kinetic energy of the emitted electron, hf is Plank's constant multiplied by the frequency of the incident photon (energy of the incident photon), and φ is the work function, which is the energy required to remove an electron from the outer surface of an atom and is generally less than 10 eV. The high gamma energies typically associated with nuclear and space environments render the energy of the work function as negligible. The energy of the emitted electron is approximately that of the incident gamma.

The angular distribution of emitted photoelectrons is dependent on the spherical harmonics and B_{LM}, a coefficient that depends on the dynamics of photoionization, the experimental geometry, the orbital from which the electron is ejected, the spatial distribution of the sample, and the photoionization energy [11]. While the angular distributions for each material can change drastically, the emitted electrons are more likely emitted in the direction of the incident photons due to the electric vector of the gammas being perpendicular to the direction vector [11].

The probability of photoelectric absorption is symbolized by τ and is shown below in Equation (4),

$$\tau \propto \frac{Z^n}{(hv)^3} \tag{4}$$

where Z is the atomic number of the absorbing matieral, n is a constant between 3 and 4, and hv is the incident photon energy. This proportionality shows that high-Z materials are more likely to exhibit photoelectron production up to energies of 1 MeV (shown in Figure 11) and have highest probability of interaction compared with other low-Z materials [12].

2.1.1.2 Compton Scattering

Compton scattering occurs between an incident gamma-ray photon and the individual electrons of the target material. The incident photon transfers a portion of its energy to the electron, known as a Compton electron. The energy of the Compton electron can range from zero up to a large fraction of the gamma energy, subject to mechanics similar to billiard ball interaction. The average percentage of energy transferred to the Compton electron increases as photon energy increases as shown according to Equation (5),

$$E_{\gamma'} = \frac{E_\gamma}{1 + (\frac{E_\gamma}{m_e c^2})(1 - cos\theta)} \tag{5}$$

where $E_{\gamma'}$ is the energy of the scattered gamma, E_γ is the original energy, m_e is the mass of an electron and θ is the scattering angle [12].

The angular distribution of Compton electrons resembles a bimodal distribution as a function of exit angle. Figure 12 shows the distribution of scattering-angle distributions of Compton electrons over commonly encountered incident energies.

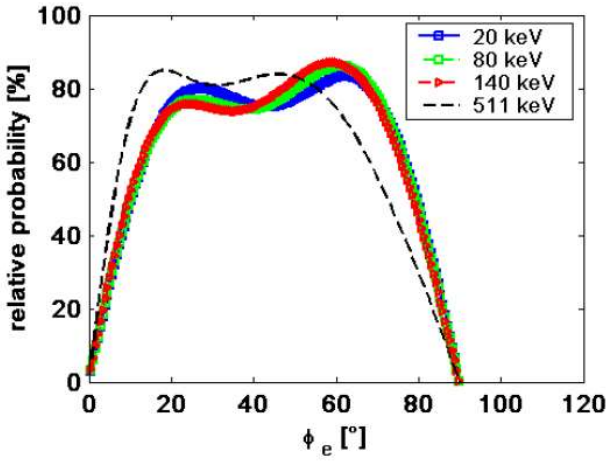

Figure 12- Scattering Angle Probability for Compton Electron from [13].

The Compton scattering probability, unlike for the photoelectric effect, is nearly independent of the atomic number [12]. The probability is directly proportional to the number of electrons per gram [12]. These factors lead to less material variance in Compton scattering probability than probability of photoelectron emission.

2.1.1.3 Pair-Production

Pair production occurs for photons with energies greater than 1.022 MeV. The incident photon interacts with the field effects from the nucleus of an atom and disappears, then reappears as a positive and negative electron pair. The energy of the electron pair is shown below in Equation (6):

$$E_{e^+} + E_{e^-} = hv - 1.022\ (MeV) \tag{6}$$

The electron and positron are emitted in opposite directions [14]. Pair production increases with increasing photon energy and increases proportionally with the square of the atomic number.

2.1.2 Electron Transport

High energy electrons produced by photon interactions lose kinetic energy through Coulomb collisions with the electrons of the target material. Electrons come to rest in the material after sufficient energy is lost. The fundamental equation that describes the energy loss during the slow down phase per unit distance travelled, or stopping power, of charged particles in matter is the Bethe-Bloch formula, [15]

$$-\langle\frac{dE}{dx}\rangle = \frac{4\pi}{m_e c^2}\cdot\frac{n\,Z^2}{\beta^2}\cdot\left(\frac{e^2}{4\pi\epsilon_0}\right)^2\cdot\left[ln\left(\frac{2m_e c^2\beta^2}{I\cdot(1-\beta^2)}\right)-\beta^2\right] \quad (7)$$

where E is the energy of the particle, m_e is the electron rest mass, c is the speed of light, n is the electron density, Z is the atomic number of the absorbing material, β is the electron velocity divided by c, e is electron charge, ϵ_0 is the vacuum permittivity, and I is the mean excitation potential. Equation (7) shows energy loss is strongly dependent on the atomic number of a medium and the velocity of the electron.

The National Institute of Standards and Technology (NIST) uses theory grounded by Bethe and the approximation that the electron is continuously slowing down (CSDA) to compute stopping powers and electron ranges in materials [16]. The NIST range of an electron in gold, silicon dioxide, silicon, and carbon (graphite) is shown below in Figure 13. The reported NIST range is normalized to density and are thus expressed in cm^2/g. Range in units of length (cm) is obtained by multiplying by the material density (g/cm^3). Figure 13 shows that electron range is similar in magnitude amongst all four of these materials if density is similar. However, range in units of cm vary according to the densities of these materials (ρ_{Au} = 19.32 g/cm^3 , ρ_{Si} = 2.33 g/cm^3 , ρ_C = 2.27 g/cm^3 , ρ_{SiO2} = 2.65 g/cm^3).

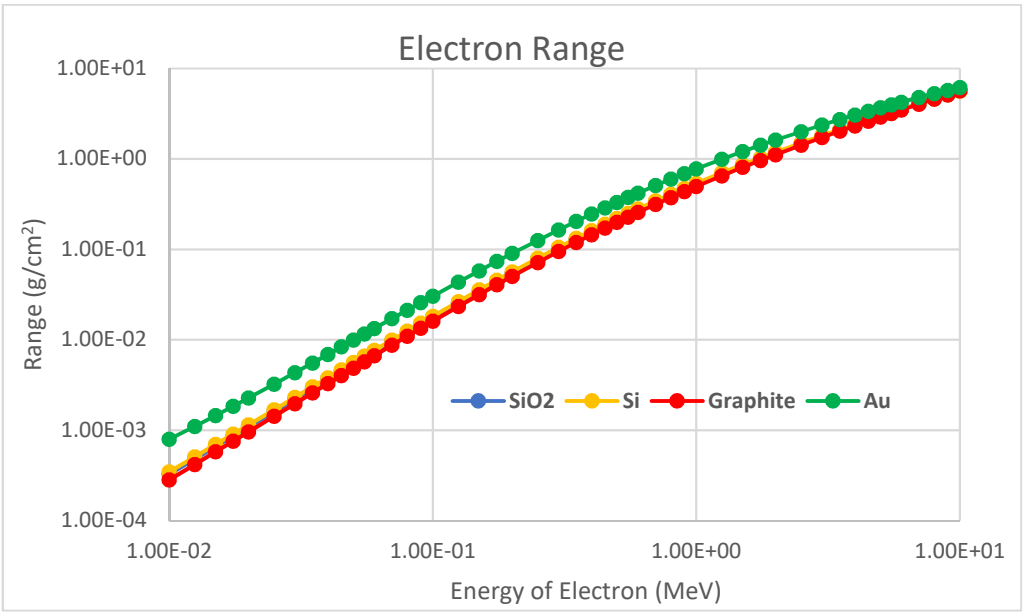

Figure 13- Range of electron in SiO_2, Si, C (graphite), and Au as a function of energy using the continuous-slowing-down-approximation from [16].

The electron range represents a 1-dimensional distance traveled in a slab and is typically far less than the total path length traveled by an electron. Electrons have small masses and are thus easily deflected travelling through matter.

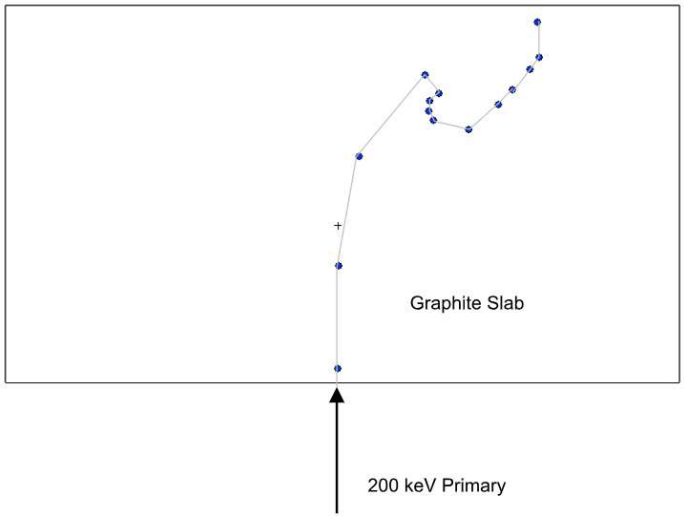

Figure 14- Electron path through a 225 µm graphite slab with initial energy of 200 keV. Blue dots represent areas where secondary "knock-on" electrons are produced with energies above 1keV. On Average for this energy electron, 14 knock-ons are produced. From [17].

Additional secondary electrons are released as the primary electron deflects along its path and are referred to as “knock-on” electrons from inelastic collisions, as shown in Figure 14. Knock-on electrons only have a very short range. Knock-ons in the case shown in Figure 14 have energies between 1-10 keV, with the majority closer to 1 keV. The range of electrons at these energies are plotted in Figure 15. A 10 keV electron has a range of approximately 1 µm, while a 1 keV electron has a range of approximately 0.01 µm [16]. Knock-ons only become relevant at the border between two different materials as electrons from one material are transported a short distance to another material.

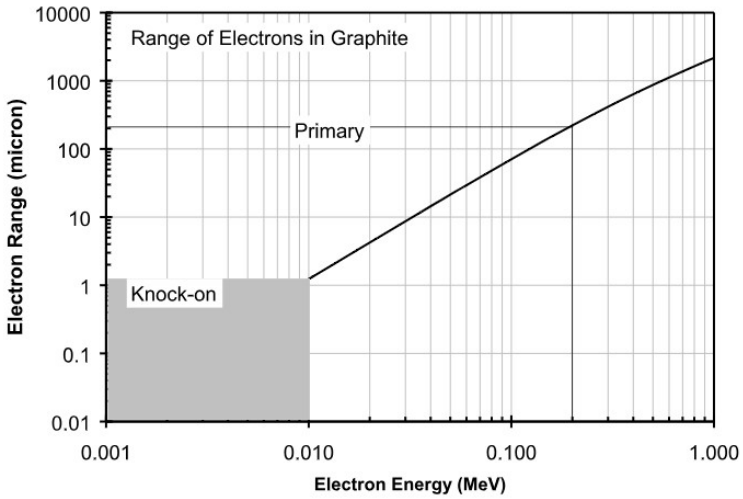

Figure 15- Range of Electrons in Graphite vs. Energy [17]

2.2 Radiation Transport Codes

The calculations of radiation effects in VacFEDs in this thesis rely on two different transport codes: CEPXS/ONEDANT and MCNP6. Both of these codes provide results in units of electron deposition or dose normalized to gamma ray source particle.

2.2.1 CEPXS/ONEDANT Transport Code

CEPXS-ONEDANT is a 1-dimensional coupled electron-photon discrete ordinates code package. CEPXS is the cross section generating code and ONEDANT is the discrete ordinate code [18], and will be referred to as CEPXS for the remainder of this thesis. CEPXS was developed by Sandia National Laboratories and generates cross sections in a multigroup-Legendre format, while ONEDANT was developed by Los Alamos National Laboratory. The discrete ordinates method uses a deterministic method for solving the Boltzmann transport equation, minimizing the computational cost for transport calculations compared to Monte Carlo methods [18].

CEPXS calculates electron/photon transport over the energy range from 1 keV to 100 MeV and uses the continuous slowing down approximation for electrons to create a multigroup-Legendre representation.

2.2.2 MCNP6 Radiation Transport Code

MCNP6 is a Monte Carlo N-Particle code that can be used for neutron, photon, electron, or coupled transport [19]. MCNP6 is the latest version of MCNP code, which is a merger of MCNP5 and MCNPX. MCNP6 will be referred to as simply MCNP for the remainder of this thesis. MCNP is developed by the Los Alamos National Laboratory and performs a 3-dimensional simulation of coupled photon-electron transport required in analyzing radiation effects on VacFEDs.

MCNP is a probabilistic code and treats an arbitrary 3-dimensional configuration of materials in geometric cells bounded by first and second degree surfaces and fourth-degree elliptical tori [19]. In these cells, the code accounts for the probability of photon and electron interactions using particular cross section evaluation. MCNP can compute electron transport for energies of 1 keV to 1 GeV and photon transport for 1 keV to 100 GeV. MCNP's stochastic methods require far greater computational power for calculations relevant to VacFEDs due to small geometry and low interaction probability. However, contrary to CEPXS, MCNP allows the investigation of 3-dimensional configuration effects in radiation response modelling of VacFEDs

The stochastic method of sampling in MCNP by nature realizes a statistical uncertainty in the resultant tallies. MCNP reports the standard relative error for each of these tallies. The standard relative error is the standard deviation of the result divided by the mean, $\frac{\sigma}{\bar{x}}$. This value will be reported in parentheses in this thesis next to all reported tallies in the results section.

2.3 Example Calculation for Direct Drive Current

In the following section, 0.01 MeV gamma rays incident on two slabs of material will be modelled to explain the basic factors governing electron production and transport and the resulting Direct Drive (DD) charge deposition, or current. The following examples represent simplified scenarios for photon-electron coupled transport between different material layers. They are included to demonstrate the factors that can create net charge imbalance and currents between layers. The computer code outputs of CEPXS and MCNP are normalized to incident gamma ray source particle and are time independent. Electrical current is defined as a rate of flow of electrical charge. Therefore, the currents calculated in

this section are by extension normalized per unit time. Source rate must be known to calculate the electrical current.

2.3.1 Case 1: Two Thin Slabs of Same Material

In the first example, two 0.05 µm thin slabs of the silicon are subject to irradiation from 0.01 MeV gammas, shown in Figure 16.

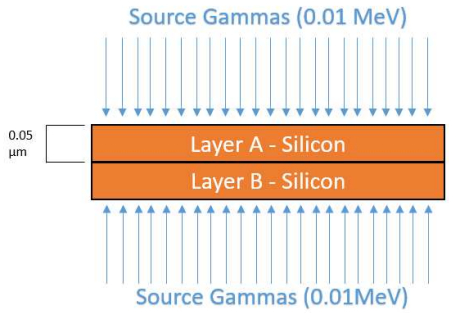

Figure 16- Model for Case 1. Two 0.05 µm silicon slabs are subject to monodirectional 0.01 MeV gamma rays.

The dominant gamma interaction mechanism is the photoelectric effect, as shown in Figure 11. Therefore, the emitted photo-electrons will have energies of approximately 0.01 MeV. NIST's electron range database dictate the approximate range of emitted electrons is approximately 1.5 µm in silicon [16]. In the photoelectric effect, the number of electrons produced is equal to the number of gammas absorbed. Using Equation (2), the number of electrons produced, becomes:

$$e^{-}{}_{prod} = 1 - \frac{I_0}{I} = 1 - e^{-\mu x} \tag{8}$$

where $e^{-}{}_{prod}$ is the number of electrons produced, I is the gamma intensity, μ is the attenuation coefficient and x is the thickness of the layer.

Since the 1.5 µm range is much greater than the thickness of material (1.5 µm >> 0.1 µm), every emitted electron is assumed to escape both slab boundaries. Each layer is expected to have a negative electron current equal in magnitude due to symmetry in geometry and gamma source. Therefore, the net current in each layer is equal to the opposite value of the number of electrons produced in each layer:

$$i_{netA} = i_{netB} = -e^{-}{}_{prod} = e^{-\mu x} - 1 \tag{9}$$

where i_{net} is the net electron current in a material.

The net currents, i_{netA} and i_{netB}, are equal and were calculated as -3.95 x 10^{-4} e^-/γ using the value of μ/ρ for silicon of 33.89 cm^2/g and a density of 2.33 g/cm^3. CEPXS was used with a monodirectional 10keV gamma source and predicted a current of -4.6 x 10^{-4} e^-/γ. MCNP with the same monodirectional 10keV gamma source predicted a value of -4.1 x 10^{-4} e^-/γ. All results are summarized in Table 1. The MCNP and CEPXS values are slightly greater due to auger electrons and knock-on electrons produced that also leave the system.

The net currents are again equal in this simple illustrative case and therefore the net direct drive is equal to zero:

$$i_{DD} = i_{netA} - i_{netB} = 0 \tag{10}$$

Table 1- Case 1 results for analytical calculation, CEPXS, and MCNP. MCNP relative standard error in parentheses.

Results for i_{netA} (e^-/γ)		
Analytical	**CEPXS**	**MCNP**
-3.95 x 10^{-4}	-4.6 x 10^{-4}	-4.0 x 10^{-4} (0.005)

2.3.2 Case 2: Two Thicker Slabs of Same Material

Case 2, shown in Figure 17, is similar to Case 1 with the thickness of the slabs increased. This demonstrates the effect of the thickness of material comparable or greater than the range of produced electrons.

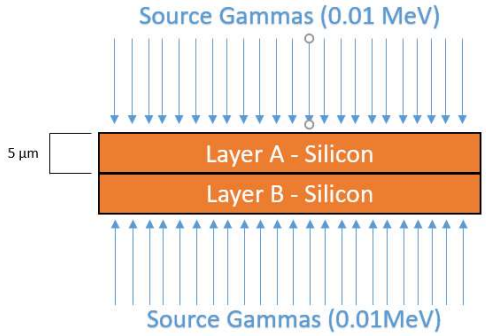

Figure 17- Model for Case 2. Two 5μm silicon slabs are subject to monodirectional 0.01 MeV gamma rays.

A large majority of the gamma rays (93%) travel unattenuated through the material, so photoelectron production is nearly equal throughout each layer. However, photo-electrons produced are subject to slowing down through collisions in the layer and may be stopped before escape. The net current in layer A is now a function of the number of electrons produced in the layer, i_{prodA}, multiplied by the average probability that a produced electron will escape, $\bar{P}_{escape}$, and as the current from layer B into layer A, i_{inB}, multiplied by the average probability that one of these electrons will be absorbed in layer A, $\bar{P}_{absorb}$:

$$i_{netA} = -i_{prodA}\bar{P}_{escape} + i_{inB}\bar{P}_{absorb} \tag{11}$$

Many factors, outlined in the previous section, determine the average probability of escape, such as the angular distribution of photoelectrons, linearity of electron path through material, electron range, and thickness of material. Likewise, the probability of electron absorption in a layer is governed by the same factors as well as initial angle entry and energy into the layer. These factors change for each electron and are probabilistic in nature, highlighting the need for Monte Carlo or discrete ordinates methods, which also account for these factors.

The net direct drive current for this scenario also remains approximately zero because of symmetry. The average net electron current of both layers was determined by CEPXS as -1.4 x 10^{-3} e^-/γ and MCNP as 1.8 x 10^{-3} e^-/γ. This value is larger than in Case 1 because the layers are thicker, and allow greater electron absorption for electrons with range less than the layer thickness. The electron deposition rate remains less than the approximate magnitude of photoelectrons produced in each layer, determined by Equation (10) as 3.9 x 10^{-2} e^-/γ, due to leakage. The thickness, 5 µm, is greater than the CSDA electron range for 0.01 MeV, which is 1.5 µm.

Table 2- Case 2 results for analytical calculation, CEPXS, and MCNP. MCNP relative standard error in parentheses.

Results for i_{netA} (e^-/γ)	
CEPXS	**MCNP**
-1.4 x 10^{-3}	-1.8 x 10^{-3} (0.06)

2.3.3 Case 3: Two Thin Slabs of Different Density

Case 3 has the same configuration as Case 1 with an increased density of Layer B, shown in Figure 18. This configuration demonstrates how changing density can cause an imbalance in electron deposition to realize a net direct drive current.

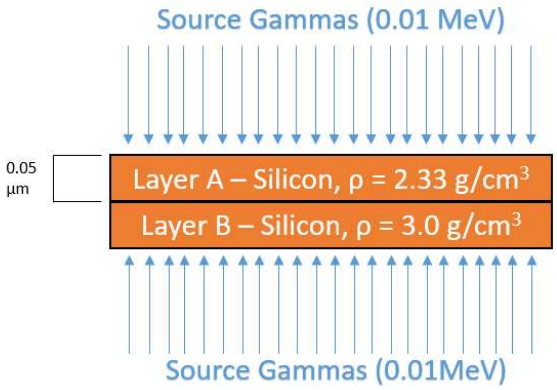

Figure 18- Model for Case 3. Two 0.05µm silicon slabs of two different densities are subject to monodirectional 0.01 MeV gamma rays.

Increasing the density affects the number of gamma interactions in the layer, as shown in Equation (10), and the range of the electrons. The values for the relevant variables in electron transport, production, and the calculated net electron current are shown in Table 3. The resultant net direct drive current for the CEPXS, 1.1 x 10^{-4} e^-/γ shown in Equation (12), is equal to that of MCNP, also included in Table 3.

$$i_{DD} = i_{netA} - i_{netB} = -0.00046\,\frac{e^-}{\gamma} + 0.00057\,\frac{e^-}{\gamma} = 1.1\,x\,10^{-4}\,\frac{e^-}{\gamma} \qquad (12)$$

Table 3- Case 3 results using CEPXS and MCNP. MCNP relative standard error in parentheses.

Layer	Density (g/cm^3)	μ (cm^{-1})	Electrons Produced in Layer (e^-/γ) $(1 - e^{-\mu x})$	CSDA Range of Electrons (cm)	CEPXS Calculated Net Electron Current (e^-/γ)	CEPXS Direct Drive Current Magnitude (e^-/γ)	MCNP Direct Drive Current Magnitude (e^-/γ)
Layer A:	2.33	78.96	3.9 x 10^{-4}	1.5 x 10^{-4}	-4.6 x 10^{-4}	1.1 x 10^{-4}	1.1 x 10^{-4} (0.03)
Layer B:	3.00	101.67	5.1 x 10^{-4}	1.2 x 10^{-4}	-5.7 x 10^{-4}		

2.3.4 Case 4: Two Thick Slabs of Different Material

Case 4, shown in Figure 19, modifies Case 2 with two different materials with different cross sections, with layer B as carbon (graphite). In order to isolate cross section as the only variable compared with Case 2, the density of carbon is artificially kept the same as for silicon. (This density is much lower than the naturally occurring density of graphite at room temperature).

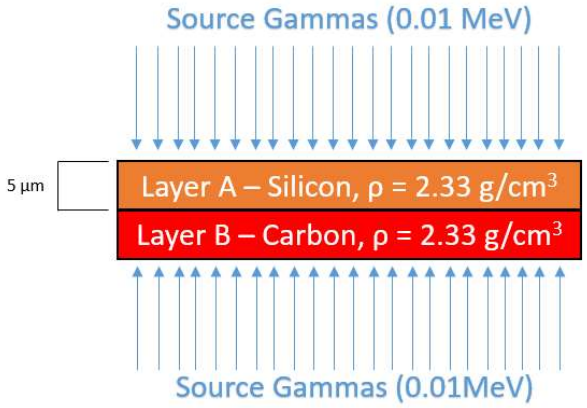

Figure 19- Model for Case 4. One 5µm silicon slab and one 5 µm graphite slab of same density are subject to monodirectional 0.01 MeV gamma rays.

Electron range, as well as attenuation probability are different for the two materials. This produces an artificially unequal net electron current in each layer and a direct drive current of 3.6 x 10^{-3} e^-/γ, greater than Case 3, as shown in Table 4. MCNP provides a significantly different result than CEPXS. The number of photon collisions was approximately 4.2 x 10^{-2} e^-/γ for both codes, suggesting differences in direct drive current results arise due to electron transport methods between the two codes.

Table 4- Case 4 using CEPXS and MCNP. MCNP relative standard error in parentheses.

Layer	Attenuation Coefficient µ (cm^{-1})	CSDA Range of Electrons (cm)	Electrons Produced in Layer (e^-/γ) $(1 - e^{-\mu x})$	CEPXS Calculated Net Electron Current, i_{net} (e^-/γ)	CEPXS Direct Drive Current Magnitude (e^-/γ) $\lvert i_{netA} - i_{netB} \rvert$	MCNP Direct Drive Current Magnitude (e^-/γ) $\lvert i_{netA} - i_{netB} \rvert$
Layer A:	78.96	1.5 x 10^{-4}	3.9 x 10^{-4}	-2.5 x 10^{-3}	3.6 x 10^{-3}	4.7 x 10^{-3} (0.005)
Layer B:	5.53	1.2 x 10^{-4}	5.1 x 10^{-4}	1.1 x 10^{-3}		

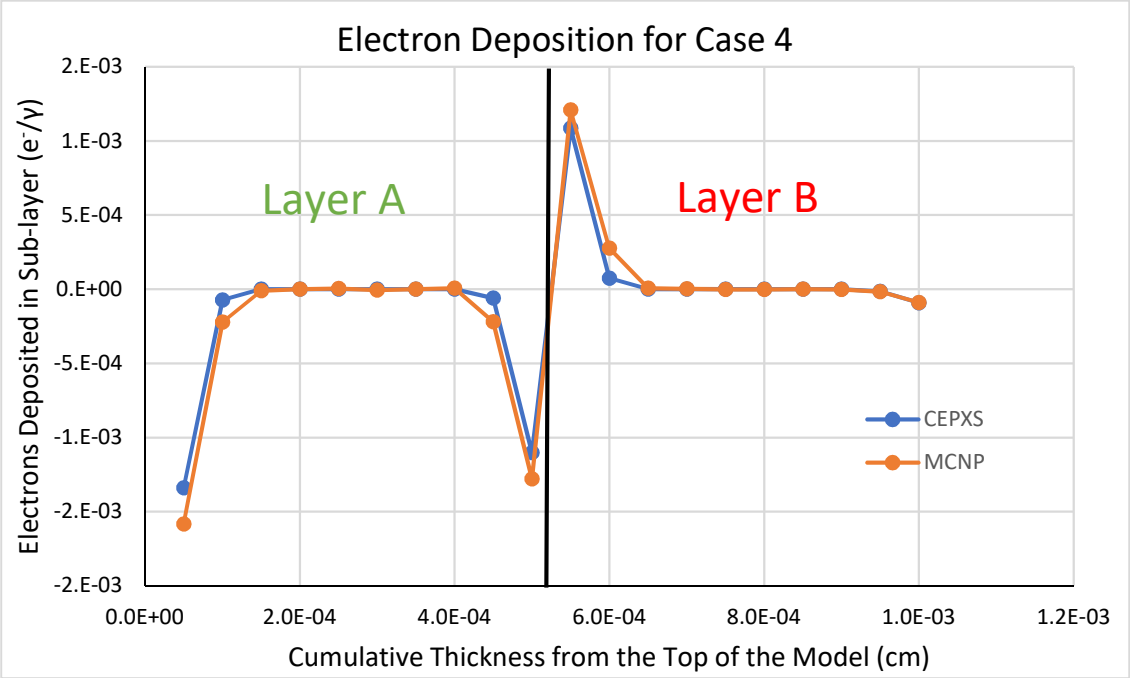

Figure 20- Net electron deposition (integral) in 0.05µm sub-layers for Case 4. The x-axis represents distance from the top of the model presented in Figure 19. Results from both CEPXS and MCNP are plotted. Error bars calculated from standard error from MCNP too small to show on Figure.

Figure 20 divides these two layers into a mesh of ten 0.5 µm sub-layers to demonstrate the differential electron deposition in the two devices. Each point represents the total number of electrons deposited in each 0.5 µm cell. Electron deposition is close to zero throughout the majority of each layer. This is because most electrons are at equilibrium between layers, meaning they do not escape the layer. Electrons escaping these sublayers are balanced by an approximately equal number incoming from other layers. Both layers exhibit a net negative number of electrons on the border surrounded by a vacuum because electrons are produced near this border and escape the material creating an overall negative current in these regions.

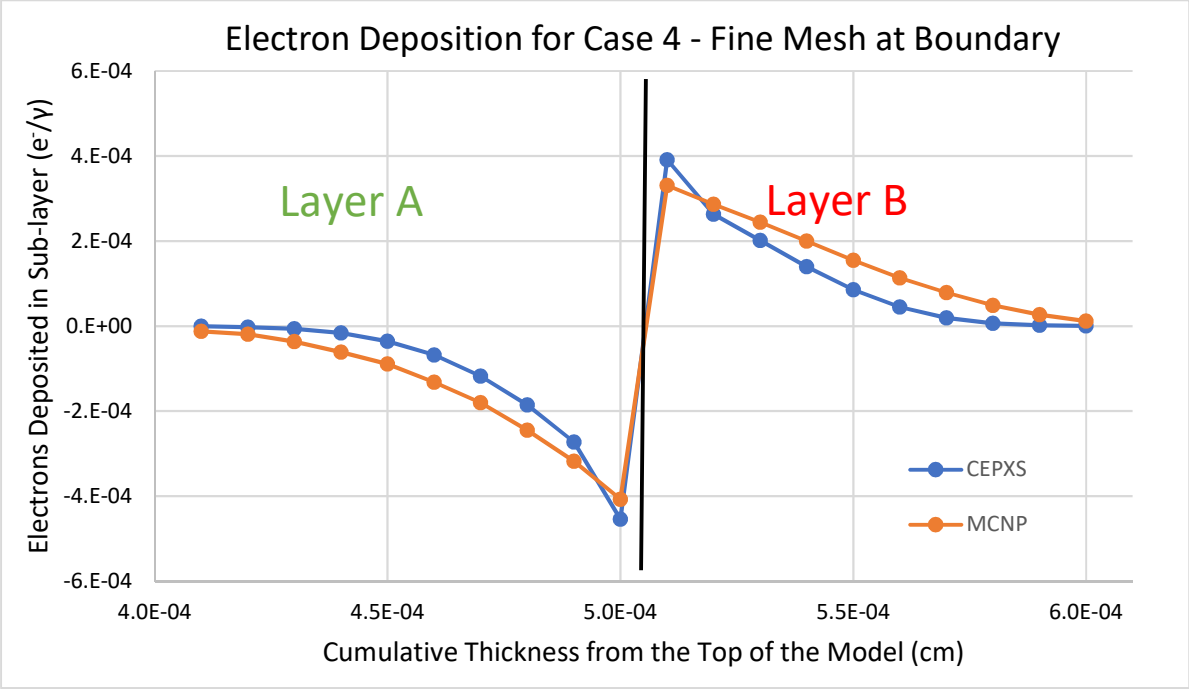

Figure 21- Net electron deposition in 0.1 µm sub-layers for Case 4 calculated using CEPXS. The x-axis represents distance from the top of the model presented in Figure 19. Only the region close to the material boundary is shown. The overall magnitude of the peak of this Figure is less than that of Figure 20 because each point in this Figure represents an integral net electron deposition over a smaller width. Direct drive current does not change with mesh refinement because the integral of the entire layer remains unchanged. Standard error from MCNP too small to show on the figure.

Figure 21 zooms in with a finer mesh of 0.1 µm sublayers on the boundary between layer A and layer B. There is an apparent imbalance in the magnitude of the electron deposition profile in each sublayer while approaching the material boundaries. This is due to the difference in cross section and imbalance in production of photo-electrons near the boundary where photo-electrons are more likely to cross into a different layer. Additionally, this effect is magnified very close the boundary where knock-on electrons have sufficient range to transport to the adjacent layer. Layer A has a far greater attenuation coefficient than layer B (reference Table 4), so many more electrons are produced with potential to travel into layer B, causing depletion in layer A and buildup in layer B. The electron ranges in these materials are comparable, so the attenuation coefficient dominates the effect in this case. The peak magnitude of Figure 21 is less than that of Figure 20 because a finer mesh resulted in a lower electron deposition in

each cell. Total direct drive current over the entire material layer does not change with mesh refinement because the integral of the entire layer remains unchanged.

2.3.5 Effect of energy

Figure 22 shows the effect of changing the energy of the incident gamma rays in Case 4 using CEPXS. Direct drive current generally decreases with increasing energy in this scenario. This trend is caused by a decrease in the attenuation coefficient of the materials, as shown in Figure 10. The initial decrease is not linear, as a prediction based purely on attenuation coefficients and the attenuation equation would predict, because the range of electrons grows beyond the dimensions of the test problem for with increasing energy (reference Figure 13 for electron ranges).

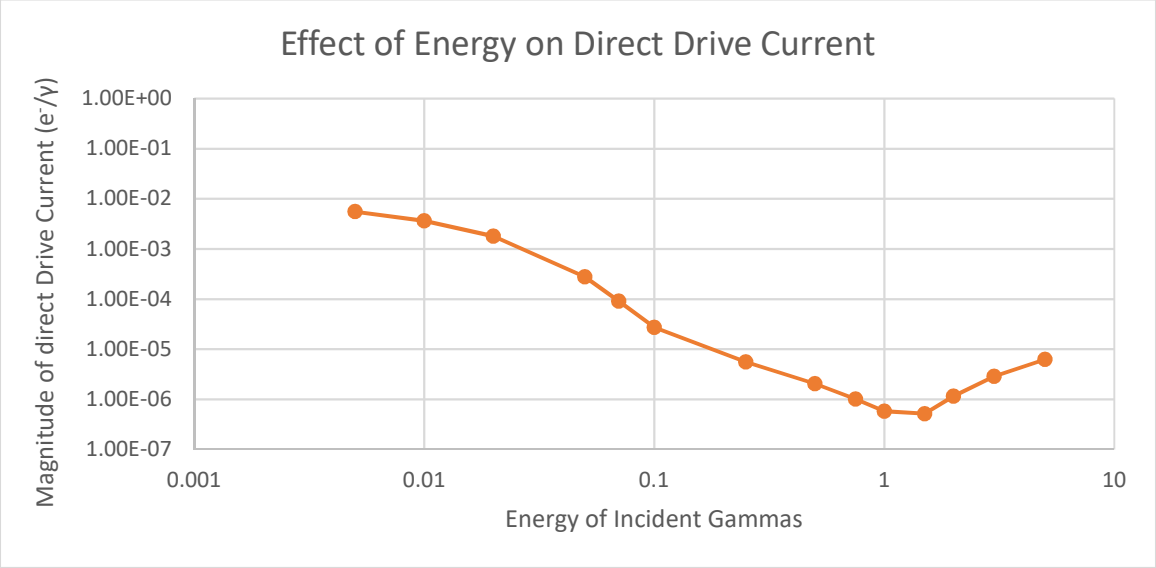

Figure 22- Direct drive current for Case 4 simulated in CEPXS with varying gamma energies.

2.4 Mitigating Direct Drive

A number of factors such as device geometry, material selection, and radiation source, identified in the previous section, affect direct drive current. Direct drive is greatest for low energy gammas in the previous examples because the materials have higher attenuation coefficients at these energies and vary greatly by material. Material selection with similar cross section and density has the greatest impact on minimizing direct drive. This is because direct drive current is driven by an imbalance of photon cross section and electron deposition between layers. Furthermore, materials with large atomic

number should be avoided because they provide large contrast in photoelectric cross sections and electron stopping powers compared with that of silicon and carbon.

2.5 Radiation Induced Conductivity

Insulating layers are critical in modern electronics because they provide dielectric isolation between conducting layers. In current prototype VacFEDs, SiO_2 is used to isolate the conducting materials of the cathode and anode from the silicon substrate [5]. Ionizing radiation can increase the number of charge carriers in an insulator held under bias, thereby making the layer more conductive through drift transport of these new electron-hole pairs. This increased conductivity is referred to as Radiation Induced Conductivity (RIC). Figure 23 is a simple representation of RIC. This section will explore RIC as a radiation effect in a VacFED, how to calculate RIC in a simple circuit system, its timescale, and ways to mitigate RIC effects.

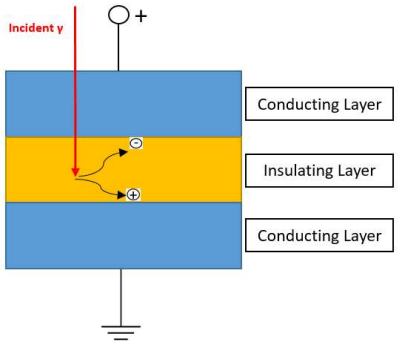

Figure 23- Representation of RIC. An incident gamma-ray creates an ionization in an insulating layer. This causes an electron-hole pair to be swept in opposite direction under bias.

2.5.1 RIC in Oxide Layer of a VacFED

It is essential to electrically isolate the conductive layers from the silicon substrate held at ground in the simplest form a VacFED diode. Figure 24(a) represents a vertical cut view of a VacFED with three potential current paths. Figure 24(b) represents this in a circuit model with three different resistors. Current 1 and resistor 1 represent the intended current across the vacuum gap. Currents and resistors 2 and 3 represent potential leakage pathways of current through the SiO_2 insulator. A voltage source is placed at the anode, with the cathode and substrate at ground.

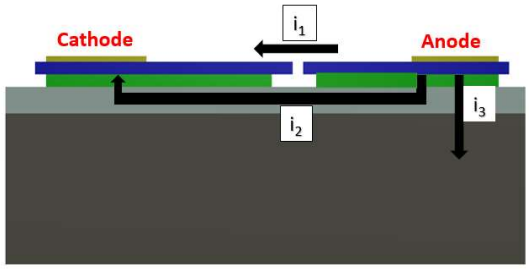

(a)

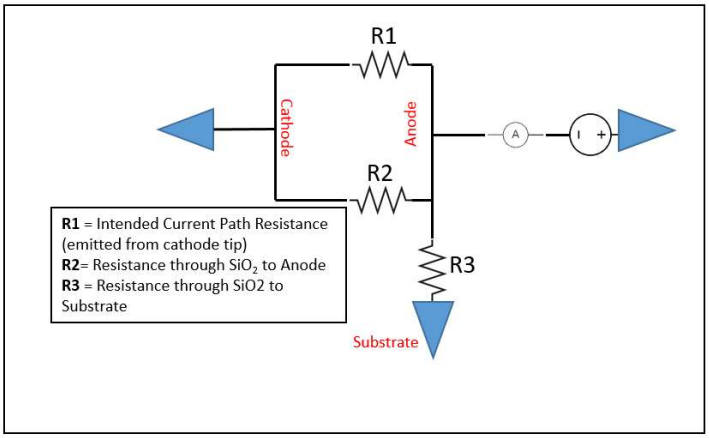

(b)

Figure 24- (a) Side view of a VacFED showing the intentional current flow, i_1, as well as potential unwanted current flow through the oxide due to voltage differentials, i_2 and i_3 (b) Simplified circuit diagram of (a). An ammeter is shown where output current would typically be measured in the simplest diode design.

The total current at the anode, i_A, is the sum of the three currents depicted, i_1, i_2, and i_3 according to Kirchoff's law. The total current at the anode from RIC sums with intended current from the cathode. Significant currents through the insulator, i_2 and i_3 represent a competing noise source. Excessive current in this leakage path can result in heating, degradation of the diamond layer, or potential overload of the surrounding circuitry.

2.5.2 Calculating Prompt RIC

RIC has both a prompt and delayed response to a pulse of ionizing radiation in a variety of insulators. Prompt RIC response has been shown in amorphous solids to follow a simple power law dependent on dose rate as: [20] [21]

$$\sigma_p(\dot{D}) = k_c \dot{D}^{\Delta} \tag{13}$$

where $\sigma_p$is the prompt RIC, $\dot{D}$ is the dose rate, k_c is a constant RIC coefficient [$\Omega^{-1}m^{-1}$/rad/s] and Δ is an exponential parameter. The parameters k_c and Δ are dependent on temperature. RIC coefficients and power law fit can change for different dose rates, as shown in Figure 25. In this scenario, pulses of either 50 ns or 500 ns were given at six different dose rates to a 10 mil fused silica film by a linear accelerator [21]. The calculated value for σ_p from pulsed experiments were used in the analysis section to determine the magnitude of RIC currents that would result from a continuous high dose rate exposure in a reactor environment.

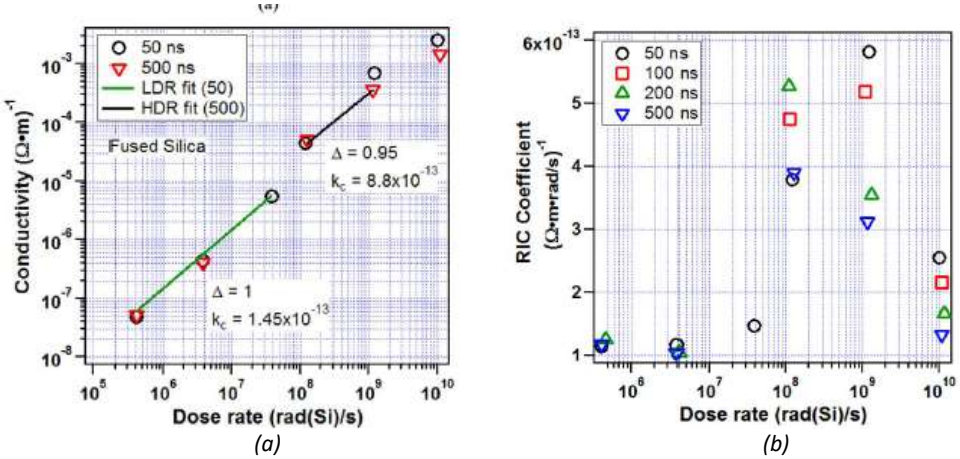

Figure 25- (a) Plot of radiation-induced conductivity vs. dose rate (b) Plot of the RIC coefficient vs. dose rate from [21]. Pulses of either 50 ns or 500 ns were given at six different dose rates to a 10 mil fused silica film by a linear accelerator.

Table 5 shows the RIC correlations that will be used for SiO_2 in the Section 3 calculations for RIC. The applicability of pulse data is discussed in the following subsection of this thesis.

Table 5- RIC Coefficients used in Device Calculations.

Dose Rate Regime [rad(Si)/s]	**k_c [1/ohm-cm]**	Δ	**Source for Constant Values**
0 - 10^4	2 x 10^{-13}	1.01	Dennison [22]
10^4 – 5 x 10^7	1.45 x 10^{-13}	1	McLain et al. [21]
5 x 10^7 – 10^{10}	8.8 x 10^{-13}	0.95	McLain et al. [21]

RIC is a function of the localized dose in the insulator. A radiation transport code is used for geometry with multiple layers and materials. MCNP and CEPXS are used in this thesis to determine the localized dose.

2.5.3 Delayed RIC and RIC under Continuous Dose Rates

RIC is primarily a prompt effect for SiO_2, meaning, the enhanced conductivity ceases after the source (pulse) of radiation is complete. Recombination of charge occurs after the radiation exposure stops in the insulating layer. Conductivity in SiO_2 recovers rapidly in this process and approaches equilibrium with its pre-radiation conductivity [23]. Contrary to SiO_2, the Al_2O_3 exhibits a clear delayed effect where the observable increase in RIC spans beyond the duration of the pulse. Figure 26(a) shows RIC response to a 100 ns pulse contrasted with Al_2O_3 in Figure 26(b) [21]. The VacFEDs investigated in this project involve only SiO_2 and delayed effects are not considered. However, these effects must be considered when designing VacFEDs with different insulating materials.

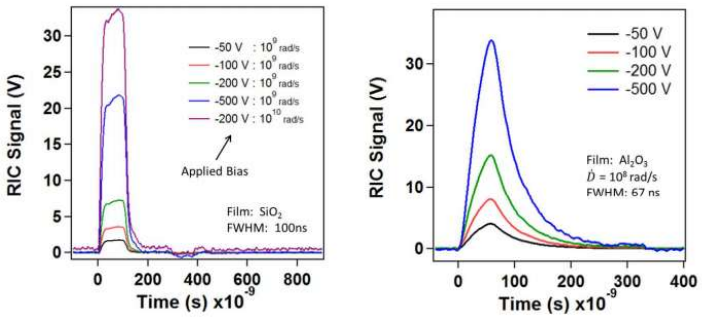

(a) (b)

Figure 26- RIC signal response to 100ns pulse widths for (a) SiO_2 (b) Al_2O_3 from [21].

In many environments, such as a nuclear reactor, there is a constant high dose rate, unlike the short pulses conducted in most RIC laboratory experiments. Previous research has shown RIC to be considerably lower for a longer pulse width at higher dose rates in SiO_2 [21]. One possible explanation is space charge effects increase the likelihood of recombination of charge carriers, thus reducing RIC over time [21] [24]. This thesis uses the prompt RIC coefficients from short pulse experiments as a upper bound for maximum RIC response in a constant high dose rate environment in the absence of continuous dose rate RIC response data.

2.5.4 Effect of Temeprature on RIC

The previously stated SiO_2 RIC correlations apply to room temperature conductivity. However thermal activation at high temperatures from shallow traps in insulators can significantly increase RIC [25] [26]. Unfortunately, limited data exists combining high dose rates with high temperatures in SiO_2. Insight can be gained from examining different insulating materials. Figure 27 shows the effect of increasing temperature on RIC in Al_2O_3. Increasing the temperature from 20℃ to 300℃, the approximate temperature of the coolant inside a light water reactor, leads to a conductivity that is approximately one order of magnitude higher for the 6.0 Gy/s and 0.6 Gy/s tests.

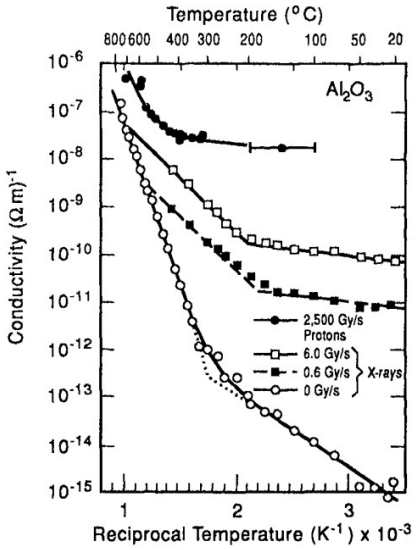

Figure 27- Electrical conductivity of polycrystalline alumina versus reciprocal temperature with and without ionizing radiation from [25].

Modern VacFEDs operate through the use of cold cathode materials [5] and are relatively insensitive to an increase in temperature of the device. However, temperature's effects on RIC should be considered in high-temperature environments, such as nuclear reactors. High-temperature environments are not considered in this study due to limited data on combined effects of temperature and RIC.

3 Modeling of Ionizing Radiation Effects on VacFEDs

The purpose of this section is to estimate radiation effects due to Direct Drive and RIC. This section focuses on diodes of four different configurations. CEPXS and MCNP are both used to simulate monodirectional incident source particles in a 1-dimensional model. Additionally, a full three-dimensional model is created in MCNP with an isotropic source distribution to simulate a radiation environment similar to that of a nuclear reactor. The results in the three different computer models are compared for four different diode configurations. Incident gammas are used for all source particles in this section.

3.1 VacFED Geometry and Material Configurations

All device configurations considered are diodes. In a VacFED diode, electrons are emitted from the cathode tip to the anode. The output current is determined by the voltage across the vacuum cathode to anode gap. The first diode considered in the models is a device configuration that was chosen because it represents a structure very close to what is fabricated at the time of this thesis project by Vanderbilt and Draper [5]. The design is also expected to have a low direct-drive response because it assumes bondpads and surrounding circuitry are sufficiently thin such that they do not enhance photo-electron emission. This device is referred to as Configuration A and is shown from a side view in Figure 28. Configuration A builds upon the Carbon-Silicon bi-layer structure in Section 2 with additional material layers that enable a functional lateral VacFED. The anode and cathode are made of a 0.5 µm microdiamond layer on top of 1.0 µm thick poly-Si. The density of the microdiamond layer is assumed to be the ideal density of diamond, 3.52 g/cm^3. The cathode and anode are insulated from the substrate by 2 µm of SiO_2. All of the above mentioned VacFED layers rest on top of 150 µm thick of Si substrate. The entire diode is surrounded by 2 mm of Si “equilibrators.” Equilibrators surround the device to balance electrons emitted from the device and minimize electron leakage from the device layers.

Figure 29 illustrates the cathode and anode layout from the top view. The cathode, excluding the tip, and anode are 100 µm x 100 µm squares. The gap between the cathode and anode is approximately 50

nm. The cathode tip length is 1.0 µm. The 1.0 µm underlying poly-Si layer is back-etched away 3 µm from the Carbon layer, creating a 97 µm x 97um square.

In this configuration, the Carbon and poly-Si directly below it are assumed electrically coupled conductive layers with the same circuit model from Figure 24(b). Sheet resistivity of grown diamond is approximately 3 ohm-cm [27]. Undoped Poly-Si is approximately 3 x10^5 ohm-cm at room temperature [28]. The difference in resistivities could result in trapped electrical charge in the Poly-Si layer and then subsequent discharge into the Carbon layer. This could be mitigated by doping the poly-Si to make it more conductive. However, this effect is not likely to significantly impact device operation because the resistivity of Poly-Si is far less than that of the insulating SiO_2 layer, with a sheet resistivity of 5 x 10^{12} ohm-cm or greater [22]. The cathode and substrate are connected to ground. The anode is held at a positive bias of 10 V and nominal on-state operational current is assumed as 1.0 µA.

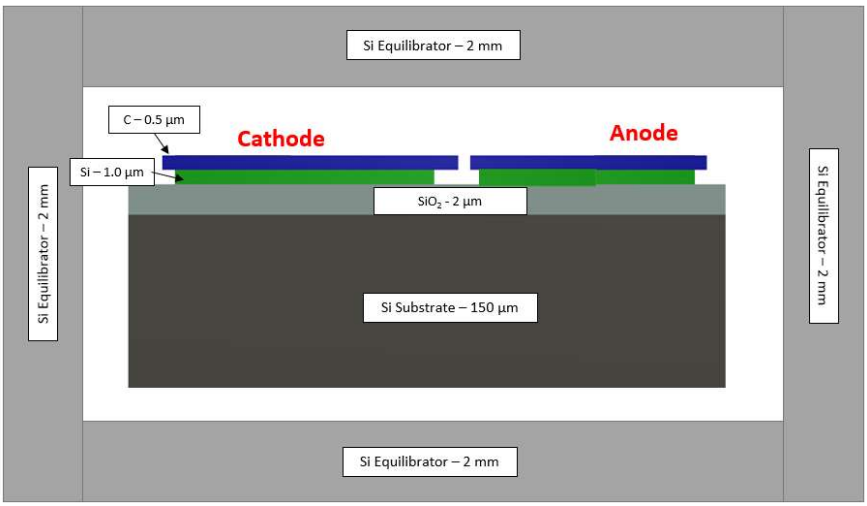

Figure 28- Side view of Configuration A VacFED. Not to Scale.

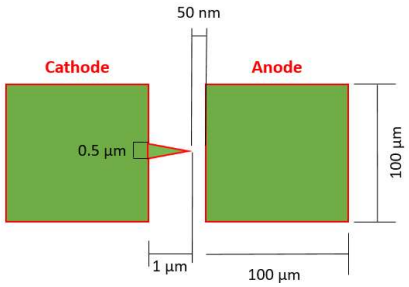

Figure 29- Top view of Configuration A VacFED. Not to Scale.

Three other VacFED diode configurations are considered in the model. Configurations A-C share the same lateral layout as depicted in Figure 28. Configuration D differs further from A-C and is described in detail later. Table 6 summarizes the differences that exist in the vertical material stack.

Table 6- Description of different VacFED configurations tested in CEPXS.

Name of Test Case	Description
Configuration A	VacFED shown in Figures 28 and 29
Configuration B	Configuration A with additional 0.5 µm Au layer bondpad above diamond layer.
Configuration C	Configuration A with additional 0.5 µm Al layer bondpad above diamond layer.
Configuration D	1-dimensional model of device to test at Draper. Has bondpad and no equilibrators. Greater surface area.

Configuration B, shown in Figure 30, features a 0.5 µm Au layer bondpad that is used to allow current flow from the anode. This scenario is considered because gold is commonly used for bondpads and has a high attenuation coefficient and density compared to the surrounding layers. The latter will cause a greater number of photo-electrons to be generated and emitted from this layer, resulting in increased direct drive charge deposition and dose into surrounding layers.

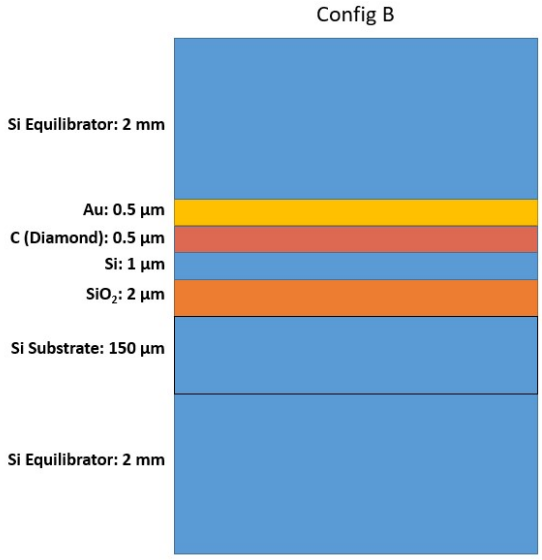

Figure 30- Configuration B in 1-dimensional representation. This is the same as Configuration A with an additional 0.5 µm Gold bondpad layer. Top view of Configuration B is same as shown in Figure 29. Not to scale.

Configuration C, shown in Figure 31, is the same as Configuration B, but has an aluminum bondpad instead of gold. This configuration is chosen to investigate whether use of a bondpad with a lower density and attenuation coefficient will significantly reduce direct drive current to levels similar to Configuration A (without bond pads).

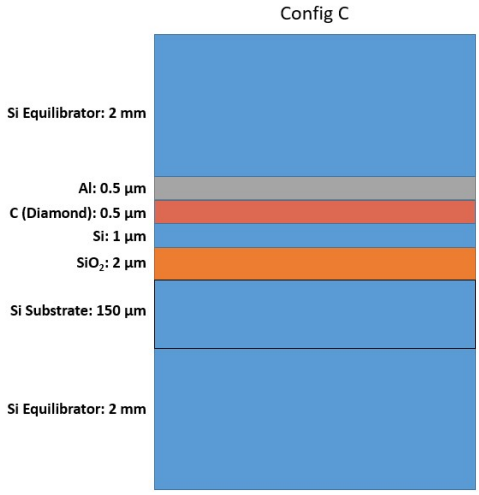

Figure 31- Configuration C in 1-dimensional Representation. The same as Configuration B, but with Al instead of Au for a bondpad. Top view of Configuration D is same as shown in Figure 29. Not to scale.

Configuration D, is closest to what is currently available in laboratory test devices without a surrounding package. It is slated for testing at Draper, and was designed largely without radiation response in mind. There are no equilibrators and highly attenuating bondpads made of three separate layers of Au, Pt, and Cr. The anode surface area is also far greater, which is expected to exhibit a greater direct drive current. Figure 32 shows the anode dimensions from a top view and Figure 33 shows the 1-dimensional side view representation. The bondpad is only above approximately half of the anode. In the 1-dimensional model, the bondpad is assumed to cover the entire surface of the VacFED with approximately half its actual thickness, as shown in the bondpad dimensions of Figure 33.

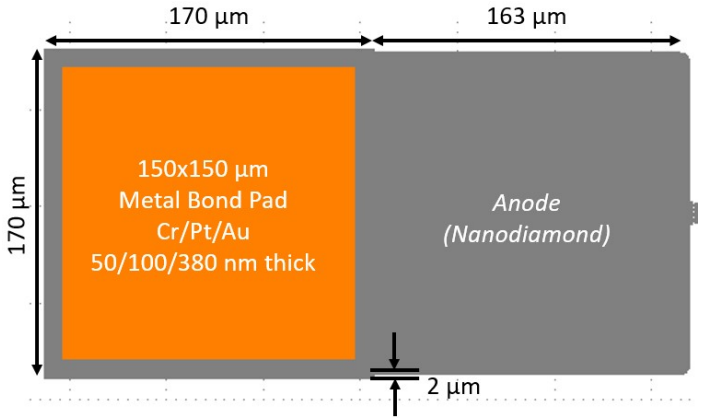

Figure 32- Top view of the anode of a Draper VacFED diode.

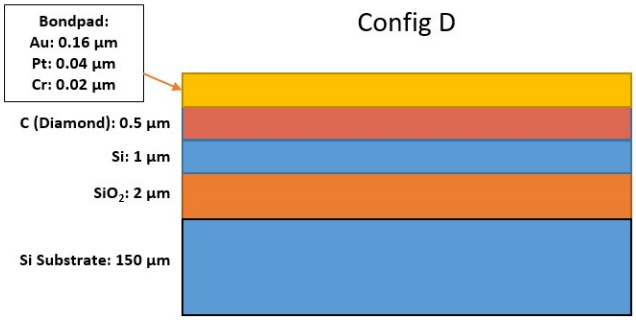

Figure 33- Side view of a Draper VacFED diode as created for a 1-dimensional simulation in CEPXS. Not to scale.

3.2 Direct Drive Current

Direct Drive current was modeled in this section using both CEPXS and MCNP. Net Direct Drive was computed from electron deposition, which was tallied in the conductive layers of the device. Three basic modelling setups were utilized. The first is a 1-dimensional model in CEPXS with mono-energetic and monodirectional gammas incident to the device surface. The second is a recreation of this 1-dimensional configuration in MCNP with monodirectional gammas. The third is a full 3-dimesional representation of a VacFED device in MCNP with gamma sources of random direction and random location outside of the device. These three modelling setups are applied to calculate direct drive for four different VacFED diode configurations, Configurations A-D.

3.2.1 Configuration A

The direct drive current for configuration A was estimated first to provide baseline data and describe the methodology of calculating the direct drive current. Configuration A is expected to have the lowest response of all other configurations due to its lack of bondpads and small geometry. Direct drive was estimated by first tallying charge deposition in the active layer and then converting into a current per unit dose rate.

Direct drive current results from an imbalance in net photoelectron absorption between the different material layers of the device in a 1-dimensional slab geometry, as demonstrated previously in section 2.3. Figure 34 shows a 1-dimensional representation of the Configuration A VacFED. Since only the anode is held at bias, as shown in Figure 24(b), and the cathode is connected to ground, the direct drive current is the net electron current in the conductive layer of the anode. Therefore, the size of the anode plays a large role in determining the magnitude of the direct drive current. The direct drive currents is presented normalized to volume of the conductive anode layers for this reason (1.5×10^{-8} cm^3 for Configuration A).

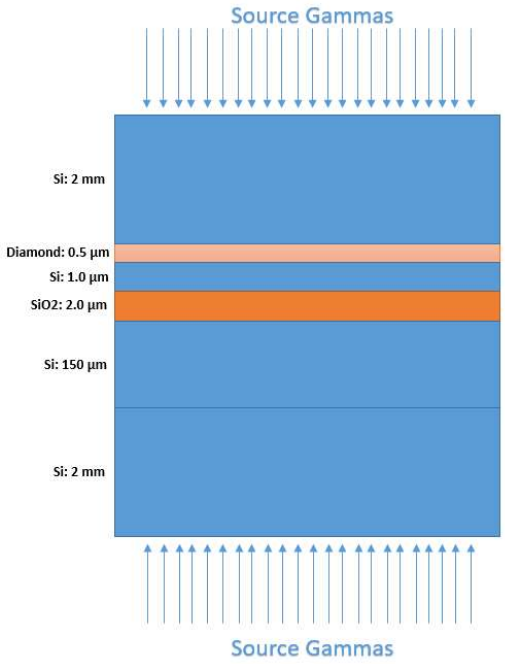

Figure 34- 1-dimensional Model of Configuration A VacFED. Not to Scale.

Source gammas coming from each direction were simulated in order to emulate source gammas incident on top and bottom sides of the device. The average of the two electron deposition values for each respective layer was used to determine direct drive current. The output from CEPXS used for a 1.0 MeV direct drive calculation with source gammas incident on the top of the device is shown below. Each value is normalized per source gamma per cm^2.

	A	**B**	**C**
	Area/Mass $(\frac{g}{cm^2})$	Dose per unit gamma source $(\frac{MeV/g}{\gamma/cm^2})$	Electron Deposition per unit gamma source $(\frac{e^-/g}{\gamma/cm^2})$
LAYER	THICKNESS (g/cm2)	DOSE (MeV-cm2/g)	Electrons-cm2/g
1	2.3300E-05	1.6197E-03	-7.5419E-02
2	4.6598E-01	2.4155E-02	-9.2982E-03
3	1.7600E-04	3.2481E-02	8.3799E-02
4	2.3300E-04	2.8359E-02	-3.1340E-02
5	5.3000E-04	3.0206E-02	1.8639E-02
6	3.4950E-02	2.8626E-02	4.4625E-05
7	4.6600E-01	2.7744E-02	-2.5415E-03

Figure 35- Electron deposition output from CEPXS for 1.0 MeV gammas incident on the top of the Configuration A device. The outlined box is a screenshot of the output. The three output columns are labeled A,B,C respectively. CEPXS normalizes units to source particle. This is not shown in the given output, but is reflected in the Figure under each column label.

The number of electrons deposited per γ in a layer, e_D, can be obtained by multiplying column A (Areal density) by column C (electron deposition per gamma fluence).

$$e_D\left[\frac{e^-}{\gamma}\right] = A\left[\frac{g}{cm^2}\right] * C\ \left[\frac{e^-/g}{\gamma/cm^2}\right] \tag{14}$$

The charge deposited per incident gamma per unit thickness, e_{DD},[C γ^{-1} cm^{-1}] is calculated by multiplying column C (electron deposition per gamma flux) by the macroscopic density of the layer.

$$e_{DD}\ \left[\frac{C}{\gamma * cm}\right] = C\ \left[\frac{e^-/g}{\frac{\gamma}{cm^2}}\right] * \rho\left[\frac{g}{cm^3}\right] * 1.6\ x\ 10^{-19}\left[\frac{C}{e^-}\right] \tag{15}$$

The incident dose per gamma fluence is determined by converting column B, the output dose into rad(Si). Incident dose is used for electronics and is conventionally determined by tallying the deposited kerma dose on the outside surface of the package and converting to rad (Si), which is 6.24E7 MeV/g per rad. Kerma is the kinetic energy released per unit mass, and is defined as the sum of the initial kinetic energies of all charged particles liberated by uncharged (gamma ray) ionizing radiation.

$$D_{inc}\left[\frac{rad}{\frac{\gamma}{cm^2}}\right] = B\left[\frac{MeV/g}{\frac{\gamma}{cm^2}}\right] * \frac{1\ [rad]}{6.24\ x\ 10^7[\frac{MeV}{g}]} \tag{16}$$

The direct drive current, i_{norm}, per unit dose rate and anode volume is calculated by dividing e_{DD} by D_{inc} and converting to Amps.

$$i_{norm}\left[\frac{A/cm^3}{rad/s}\right] = e_{DD}\ \left[\frac{C}{\gamma * cm}\right] \div D_{inc}\left[\frac{rad}{\frac{\gamma}{cm^2}}\right] * \left[\frac{A}{C/s}\right] \tag{17}$$

The dose rate required for a 0.1 µA direct drive current, previously proposed as an upper limit for noise as 10% of typical device operation, $\dot{D}_{0.1\mu A}$ is calculated by dividing 0.1 µA by i_{norm} multiplied by the anode volume, V_A.

$$\dot{D}_{0.1\mu A}[\frac{rad}{s}] = 0.1\ [\mu A]\ \div \left(i_{norm}\left[\frac{A/cm^3}{rad/s}\right] * V[cm^3] \right) \quad (18)$$

Table 7 presents an example calculation for the 1.0 MeV gamma case for all of the above figures of merit. The 1.0 MeV case was chosen since this is comparable to the gamma energies found in a reactor environment. The direct drive current per dose rate and the dose rate required for a 0.1 µA current were estimated for incident monoenergetic gamma ray energies of 30keV – 2MeV and are plotted in Figures 36 and 37. The dose rate used for these figures is the kerma dose at the surface [rad(Si)/s]. For comparison, the dose rate in the center of PWR power reactor is approximately 3 x 10^5 rad/s. Appendix B shows how this approximate dose rate is determined. A 3 x 10^5 rad/s source of 1 MeV gamma rays would produce a 6 x 10^{-8} µA direct drive current.

Table 7- Direct Drive Current Calculations for 1-dimensional Configuration A VacFED with monodirectional, monoenergetic, 1 MeV Gamma Source using CEPXS.

Forward Direction e_D [e^-/γ] in Conductive Layer	**Reverse Direction e_D[e^-/γ] in Conductive Layer**	e_{DD} $\left[\frac{C}{\gamma * cm}\right]$	$D_{inc}\left[\frac{rad}{\frac{\gamma}{cm^2}}\right]$	$i\left[\frac{A}{\frac{rad}{s}}\right]$	$i_{norm}\left[\frac{A/cm^3}{\frac{rad}{s}}\right]$	$\dot{D}_{0.1\mu A}[\frac{rad}{s}]$
7.2 x 10^{-6}	5.9 x 10^{-6}	6.9 x 10^{-21}	4.6 x 10^{-10}	2.3 x 10^{-19}	1.5 x 10^{-11}	4.4 x 10^{11}

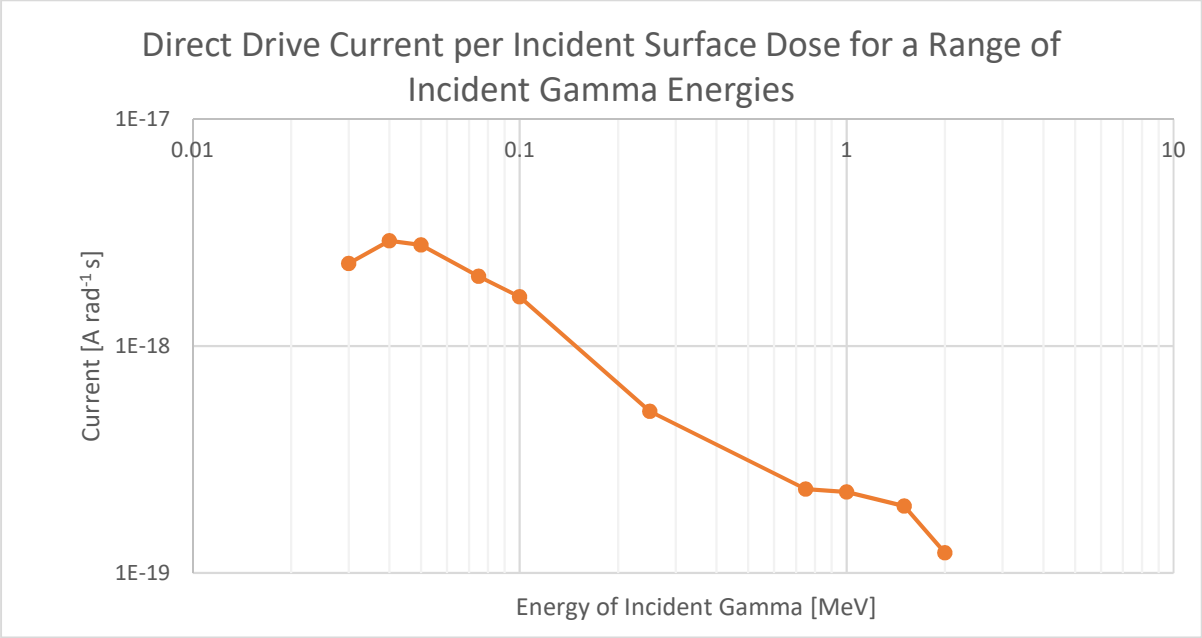

Figure 36- Direct drive current for monoenergetic incident gamma rays of various energies on the Configuration A diode using 1-dimensional model in CEPXS. Current is normalized to incident surface kerma.

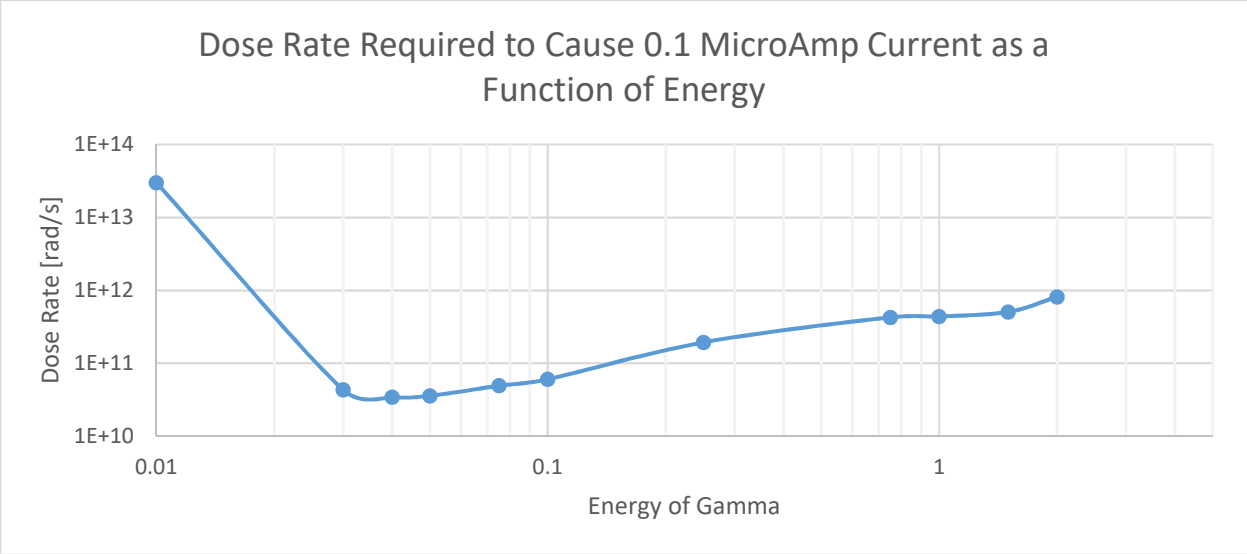

Figure 37- Gamma dose rate (surface kerma) necessary to create a 0.1 µA direct drive current for 1.0 MeV incident gamma rays on the Configuration A diode using 1-dimensional model in CEPXS.

The above CEPXS derived estimates for direct drive were validated by using MCNP by creating a 1-dimensional representation in the code. A monodirectional and monoenergetic point source was incident on the same material stack-up and sufficiently wide laterally such that no electrons escape in

the horizontal plane. The total electron charge deposited in each layer was tallied to determine direct drive current. Configuration A is used for code verification and shown in Figure 38.

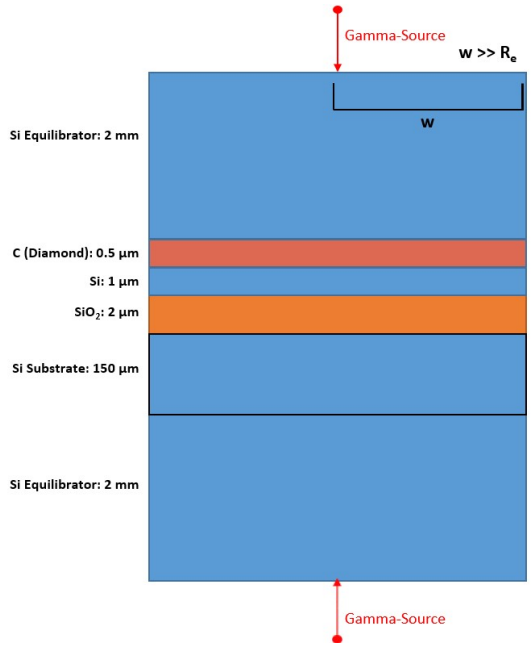

Figure 38- Recreation of 1-dimensional scenario in MCNP. A single point gamma source produces monodirectional gamma rays perpendicular to the surface on both sides of the 1-dimensional model diode. The width of the slab used, w, is far greater than the range of electrons produced in each material, R_e. This is in order to prevent leakage from the sides of the model.

A total of 2 x 10^9 source particles were simulated in MCNP to obtain statistics of less than 10% relative standard error. Electron deposition data was gathered using a +F8 charge deposition tally with units of electron charge per incident source particle. Table 8 compares the electron deposition in the conductive layers (0.5 µm C and 1.0 µm Si layer). Simulations were run for both the 0.1 MeV and the 1.0 MeV cases. The differences between the two calculations show the physical calculations of electron transport differ between the two software programs. The CEPXS direct drive current is greater for both energies, supporting its use for proposing conservative, upper bound tolerances for device operation. Differences due to source particle orientation are further explored in Appendix A.

Table 8- Comparison electron deposition results between CEPXS and MCNP for the 1-dimensional representation with both 0.1 and 1.0 MeV gamma ray sources. Relative standard error for MCNP is reported in parentheses.

	0.1 MeV			1.0 MeV		
Layer	$e_D[e^-/\gamma]$ **from MCNP6**	$e_D[e^-/\gamma]$ **from CEPXS**	**% Difference**	$e_D[e^-/\gamma]$ **from MCNP6**	$e_D[e/\gamma^-]$ **from CEPXS**	**% Difference**
C	8.69 x 10^{-6} (0.02)	1.04 x 10^{-5}	26%	1.03 x 10^{-5} (0.02)	1.39 x 10^{-5}	26%
Si	-2.21 x 10^{-6} (0.08)	-2.93 x 10^{-6}	39%	-5.96 x 10^{-6} (0.04)	-7.41 x 10^{-6}	20%
C + Si (Conductive layers)	6.48 x 10^{-6} (0.03)	7.43 x 10^{-6}	13%	4.32 x 10^{-6} (0.07)	6.48 x 10^{-6}	33%

3.2.2 Configurations B, C, and D

The same methodology for predicting direct drive response in Configuration A is repeated for configurations B-D to demonstrate how design choices can affect direct drive current, particularly with metallization layers. For each of these configurations, the direct drive current per dose rate and the dose rate required to produce a noise current of 0.1 µA are computed in CEPXS and are shown in Figures 39 and 40 respectively. The dose rate required to achieve 0.1 µA for Configurations A and C are far greater than those required by B and D. The increase in direct drive current in Configuration B is due solely to the increased photo-electrons produced and transported from the gold bondpad. This is evident because the inclusion of the gold layer is the only difference between Configuration B from Configuration A. The combination of metal bondpads, increased anode size, and lack of equilibrators, creates even more direct drive current in Configuration D.

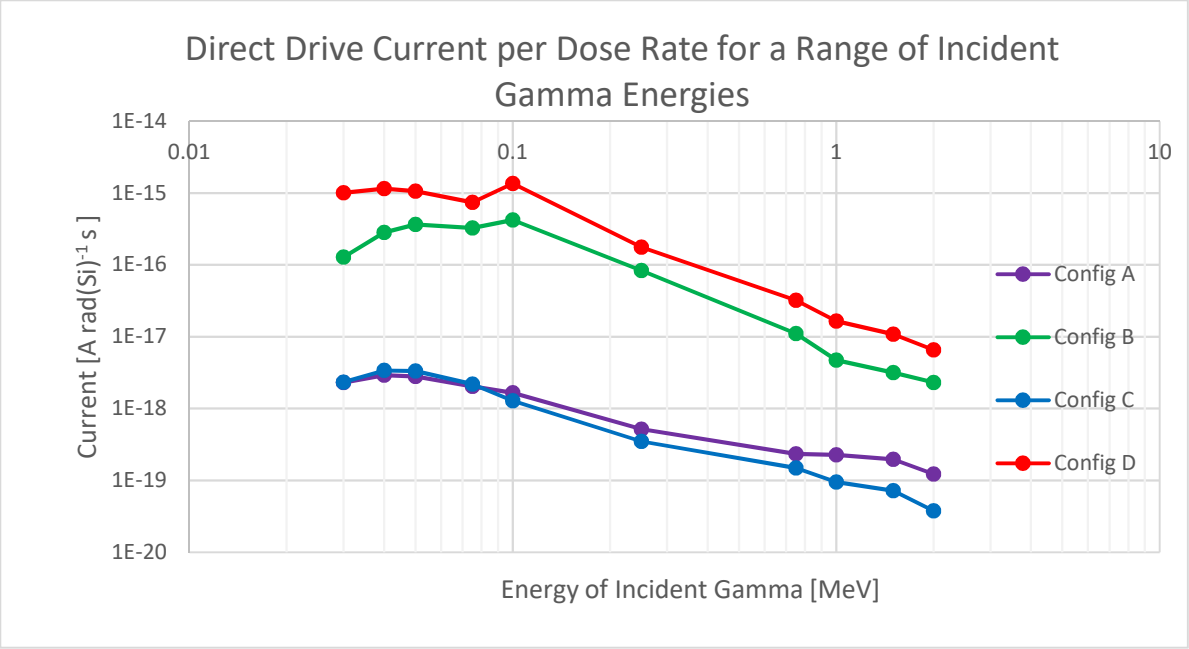

Figure 39- Direct drive current per incident dose rate for all four configurations.

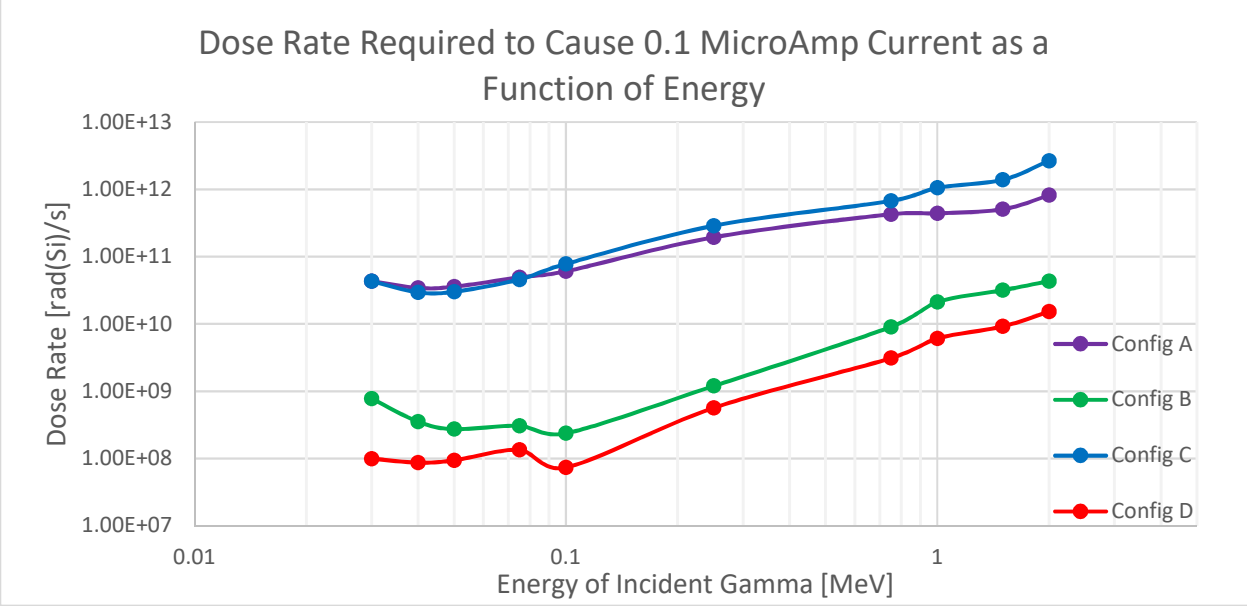

Figure 40- Dose rates required to create 0.1 µA Current as a Function of Energy for the four different configurations presented. Configuration D clearly has the greatest direct drive current over the entire spectrum of energies shown.

3.2.3 3-Dimensional Transport Validation of Configurations B and D

CEPXS-derived results were also compared to MCNP for Configurations B and D. A full 3-dimensional simulation was generated in MCNP with surrounding monoenergetic 0.1 MeV gamma isotropic point sources randomly distributed in a volume. The objective of this 3-dimensional model was not to recreate CEPXS results, as in the scenario depicted by Figure 38, but rather to simulate a scenario more similar to that of a nuclear reactor. This energy and Configs B and D were chosen because they create the largest direct drive current, as shown in Figure 40, and thus require less computation power for obtaining reasonable statistics. Figure 41 represents the basic setup for Configuration B in MCNP. Randomly distributed monoenergetic isotropic point sources in the surrounding volume were used to create gammas incident the device in all directions. In order to compare results of this model to the 1-dimensional models, the direct drive response was normalized to the dose rate incident the device, D_{inc}, which is defined as the kerma incident the surface of the VacFED $\left[\frac{MeV}{g*\gamma}\right]$. This value is obtained using an F6 cell tally at the surface. Charge deposition, $e_D\left[\frac{e^-}{\gamma}\right]$, is tallied using a +F8 tally summing the cells in the conductive layers. Equation 19 shows how this calculation is computed.

$$\dot{D}_{0.1\mu A}\left[\frac{Rad}{s}\right] = \frac{0.1\ x\ 10^{-6}\ [A] * D_{inc}\left[\frac{MeV}{g*\gamma}\right]}{6.24\ x\ 10^{7}\ \left[\frac{MeV/g}{Rad}\right] * e_D\left[\frac{e^-}{\gamma}\right] * 1.6\ x\ 10^{-19}\left[\frac{C}{e^-}\right] * 1\left[\frac{A*s}{C}\right]} \tag{19}$$

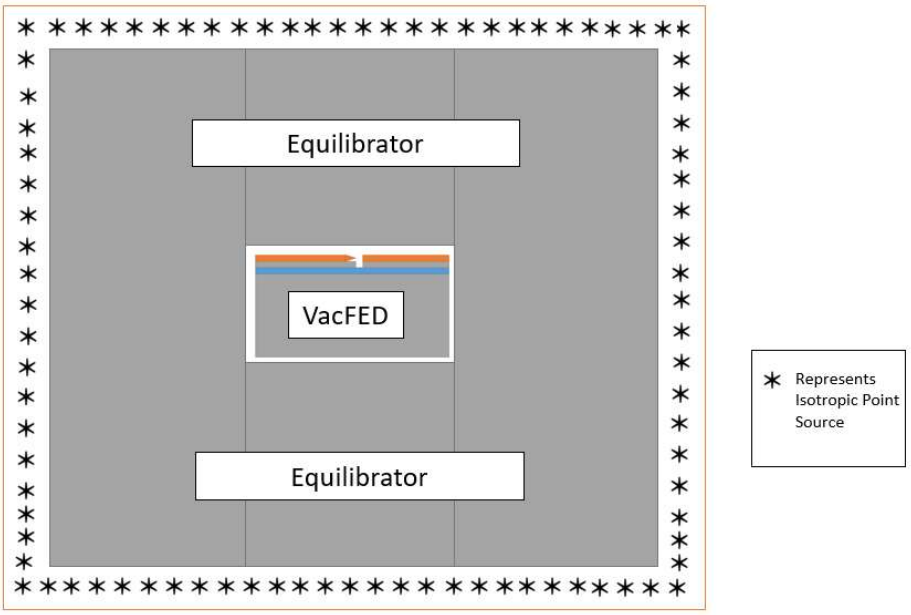

Figure 41- Simple diagram of the 3-dimensional MCNP model constructed for Configuration B. Random isotropic point sources are distributed in a small volume at the surface of the device to create source gammas from all directions. Isotropic sources are used in contrast to the monodirectional sources of the two previous 1-dimensional models presented in order to assess applicability of 1-dimensional results to a 3-dimensional scenario similar to that found in a nuclear reactor.

Table 9 provides results that compare the results from the MCNP to CEPXS for Configurations B and D. MCNP results are within 30% of the CEPXS and predicts a greater $\dot{D}_{0.1\mu A}$ for both circumstances. This strengthens the validity of using CEPXS calculations as a conservative upper bound estimate for direct drive calculations. Additionally, the difference in $\dot{D}_{0.1\mu A}$ between the full 3-dimensional MCNP model with isotropic point sources in a volume from the MCNP 1-dimensional model (Figure 38) were not statistically significant. This suggests that the direction of the incident radiation on the package does not have a significant effect when results are normalized to incident dose on the surface of the VacFED package.

Differences in electron deposition rate in the cathode versus the anode in both cases were not statistically significant in both configurations. Appendix A discusses potential differences arising from cathode geometry.

Table 9- Comparison of full-3-dimensional results from MCNP (Figure 41) to 1-dimensional CEPXS (Figure 34) and 1-dimensional MCNP recreation (Figure 38) results for Configurations B and D.

Configuration	CEPXS $\dot{D}_{0.1\mu A}[\frac{rad}{s}]$	MCNP 1-D Recreation $\dot{D}_{0.1\mu A}\left[\frac{rad}{s}\right]$	Full 3-D MCNP $\dot{D}_{0.1\mu A}[\frac{rad}{s}]$	% Difference Full 3-D from CEPXS	% Difference Full 3-D from MCNP 1-D Recreation
B (Configuration A Device with Gold Layer)	2.37 x 10^8	2.68 x 10^8 (0.01)	2.62 x 10^8 (0.02)	11%	2%
D (Draper test Device)	7.37 x 10^7	9.27 x 10^7 (0.01)	9.74 x 10^7 (0.07)	32%	5%

3.3 Radiation Induced Conductivity Current

The RIC effect is driven by the total dose rate within the insulating layer, as discussed in the theory section. Computer codes (CEPXS and MCNP) were used to estimate the dose in the insulating layer per incident photon. The incident dose rate for RIC calculations is defined as kerma at the surface [rad(Si)/s]. This is the same as D_{inc} from direct drive calculation and in Equation (16). This enables comparison of the magnitude of the two different currents. The ionizing dose experienced in the insulating layer is not necessarily the same as the dose experienced at the surface of the device. CEPXS and MCNP were used to determine the localized dose in the insulating layer of the device.

3.3.1 Configuration A

A 1.0 MeV monoenergetic incident photon scenario is first demonstrated to show methodology of RIC calculation for Configuration A. The illustration of the material stack and lumped circuit model, Figure 16 is reintroduced as Figure 42 for ease of reference. The relevant geometries in calculating RIC are shown in Table 10.

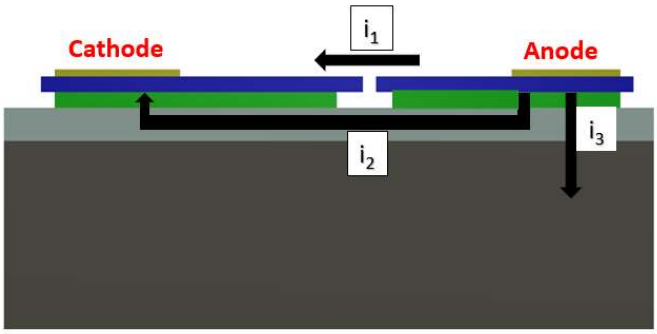

(a)

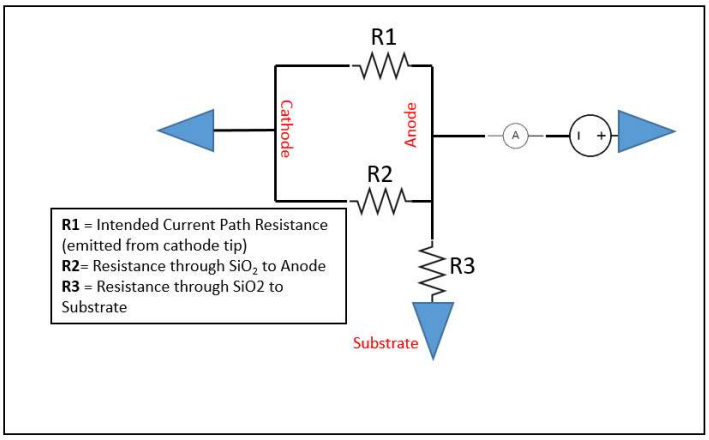

(b)

Figure 42- (a) Side view of a VacFED showing the intentional current flow, i_1, as well as potential noise current flow through the oxide due to voltage differentials, i_2 and i_3 (b) Simplified circuit diagram of (a). An ammeter is shown where output current would typically be measured in the simplest diode design.

Assuming uniform flow of electric current through the insulators (2) and (3), the resistance of R_2 and R_3 can be determined from the resistance in Equation (20). Resistivity is given as a function of dose rate due to RIC,

$$R = \rho(\dot{D})\frac{l}{A} = \frac{l}{A*\sigma(\dot{D})} \tag{20}$$

where R is the electrical resistance of the layer, ρ is the resistivity, σ is the conductivity, $\dot{D}$ is the dose rate, A is the cross-sectional area, and l is the length in the insulating layer. Kerma dose in the insulating

layer was normalized to silicon (rad(Si)/γ) at the surface of the package similar to the direct drive calculation. For example, if the calculated dose at the surface of the package is 1 rad, but the dose deposited in the insulating layer is 2 rad, the dose rate used in calculating RIC effects per unit dose incident on the device must be multiplied by 2. Therefore Equation 20 becomes:

$$R = \rho\left(\frac{\dot{D}_{SiO_2}}{\dot{D}_{Surface}}\right)\frac{l}{A} \tag{21}$$

The dose rate in the insulating layer, $\dot{D}_{SiO_2}$ [rad(Si)], is determined by obtaining the dose in the SiO_2 layer. Using CEPXS for the 1.0 MeV case, $\frac{\dot{D}_{SiO_2}}{\dot{D}_{Surface}}$ is approximately 1.0 because gamma attenuation and differences in material cross sections in the stackup are small. Ohm's law can then be used to calculate the current experienced as a result of RIC, assuming a voltage of 10 V is used, which is a target operating voltage for low voltage electronic applications:

$$i_{RIC} = \frac{V}{R(\dot{D})} \tag{22}$$

where i_{RIC} is the current due to RIC. Estimates for RIC currents i_2 and i_3, shown in Figure 42(a), for the 1.0 MeV case are presented in Table 10. Since the dose rate must be known to calculate the conductivity/resistivity, a rate of 10^6 rad/s is used in the sample calculation. The final column presents the estimated 1-dimensional direct drive current for the same source strength for comparison. The i_3 current is 50 times greater than i_2, but still much lower than the typical operational current of 1.0 µA The estimated direct drive current is far less than the RIC current in this case.

Table 10- RIC calculations for the two current pathways shown in Figure 42. The final row represents the direct drive current that would arise as a result of the same radiation source of 10^6 rad/s 1.0 MeV gamma rays.

	Current Pathway 2	**Current Pathway 3**
$\boldsymbol{V}$ **[Volts]**	10	10
$\boldsymbol{l}$ **[m]**	1×10^{-6}	2×10^{-6}
$\boldsymbol{A}$ **[m²]**	2×10^{-10}	2×10^{-8}
$\boldsymbol{\dot{D}_{Package}}$ **[rad(Si)/s]**	10^6	10^6
$\frac{\dot{D}_{SiO_2}}{\dot{D}_{Package}}$	1.0	1.0
$\boldsymbol{k_c}$ **[1/ohm-m]**	1.45×10^{-13}	1.45×10^{-13}
Δ	1.0	1.0
$\boldsymbol{\sigma(\dot{D})}$ **[1/ohm-m]**	1.45×10^{-7}	1.45×10^{-7}
$\boldsymbol{R}$ **[Ohms]**	3.45×10^{10}	6.9×10^{8}
$\boldsymbol{i_{RIC}}$ **[μA]**	2.90×10^{-4}	1.45×10^{-2}
$\boldsymbol{i_{DD}}$ **[μA]**	2.3×10^{-7}	2.3×10^{-7}

Figure 43 plots the RIC current from Equation (22) for a range of dose rates for current pathways 2 and 3. Current pathway 3 always produces a greater RIC response because the geometries relevant to Equation (20) remain constant. A noticeable jump at 5×10^7 rad(Si)/s in RIC response is due to a change in the RIC coefficient used to fit higher dose rates. The RIC coefficients used can be found in Table 5 of Section 2.

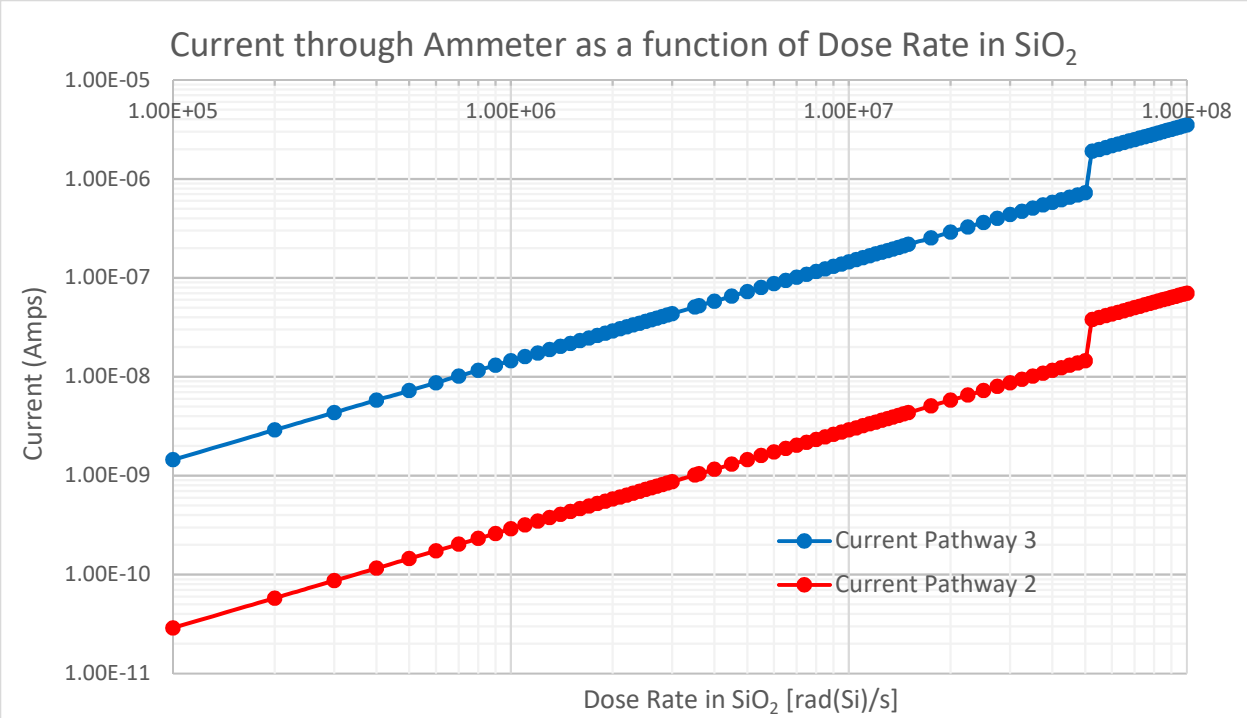

Figure 43- This Plots the primary RIC current per incident dose in SiO_2. The large jump at 5 x 10^7 rad(Si)/s in RIC response is due to a change in the correlation used. The relevant correlations are shown previously in Table 5.

3.3.2 RIC in Configurations B, C, and D:

RIC current was also computed for all four configurations introduced in Table 11 through current pathway 3 for a 10^6 rad/s source of 0.1 MeV photons.. A 0.1 MeV gamma source was chosen because the attenuation values of the materials involved changes greater for this energy than for 1.0 MeV gammas. The four different configurations produced different RIC due to changes in $\frac{\dot{D}_{SiO_2}}{\dot{D}_{Surface}}$ and the surface area of the device. $\frac{\dot{D}_{SiO_2}}{\dot{D}_{Surface}}$ is much greater in configurations B and D due to enhanced dose from electrons emitted from metal bondpads. Surface area is the same for configurations A-C, but greater for D.

Table 11- RIC current due to a 10^6 rad(Si)/s 0.1 MeV gamma source for the four configuration introduced in the previous section. The final column represents the direct drive current that would arise as a result of the same radiation source.

Configuration	l [m]	A [m²]	$\frac{\dot{D}_{SiO_2}}{\dot{D}_{Surface}}$	$\sigma(\dot{D})$ [1/ohm-m]	R [Ohms]	RIC Current i_{RIC} [µA]	Comparable Direct Drive Current i_{DD} [µA]
A	2×10^{-6}	2.0×10^{-8}	1.1	1.60×10^{-7}	6.25×10^{8}	1.60×10^{-2}	1.65×10^{-6}
B	2×10^{-6}	2.0×10^{-8}	3.6	5.22×10^{-7}	1.92×10^{8}	5.22×10^{-2}	4.20×10^{-4}
C	2×10^{-6}	2.0×10^{-8}	1.0	1.45×10^{-7}	6.90×10^{8}	1.45×10^{-2}	1.28×10^{-6}
D	2×10^{-6}	1.1×10^{-7}	2.0	2.90×10^{-7}	6.27×10^{7}	1.59×10^{-1}	1.36×10^{-3}

Configurations B and D have a far greater RIC current than C and A. Configuration B has a greater RIC current because the metal bondpads enhance electron generation and dose in the SiO_2. Configuration D has the greatest RIC current due to two factors. First, similar to Configuration B, the bondpad creates electrons that deposit greater dose in the SiO_2. Second, the surface area of the device is far greater, leading to a decreased resistance for RIC current. RIC current dominates over direct drive for all VacFED configurations.

Figure 44 plots the RIC current per incident dose rate along with the direct drive current over a range of energies for all four configurations. The RIC coefficients used in Figure 44 correspond to dose rates between 10^4 rad/s and 5×10^7 rad/s from Table 5. Figure 45 is a plot of the dose rate required to cause a 0.1 µA current due to both RIC and direct drive over a range of energies for all four configurations. Results are obtained in both figures from monoenergetic and monodirectional incident photons. For each configuration, RIC response dominates over direct drive.

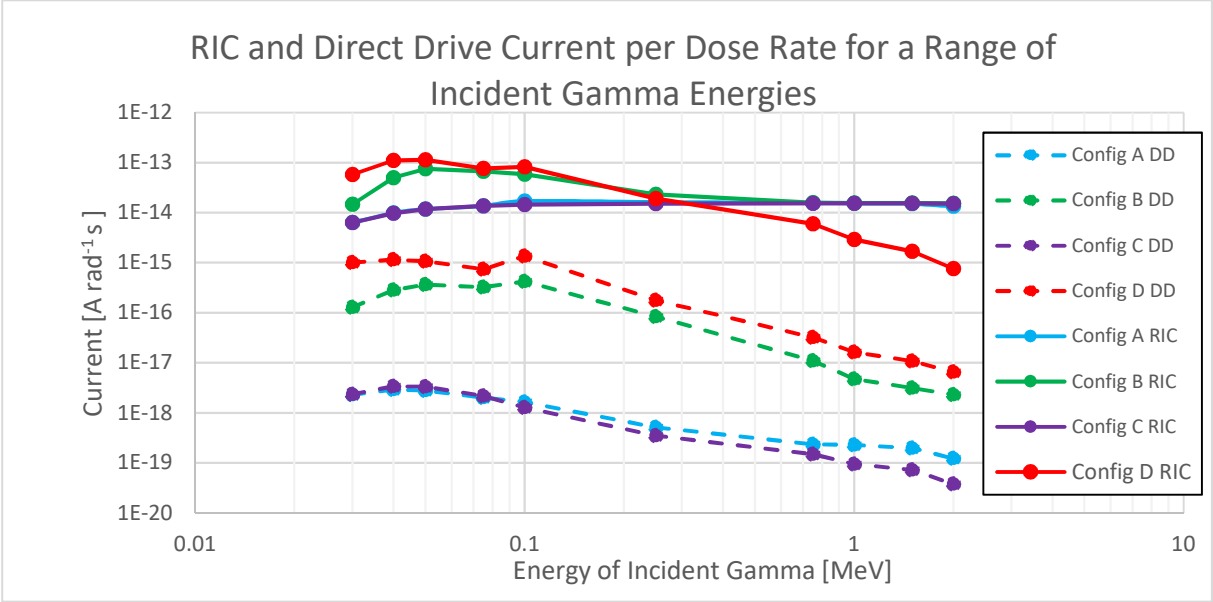

Figure 44- RIC and Direct drive per incident dose rate in all four configurations. All simulations were run with monodirectional and monoenergetic gammas in CEPXS. Direct drive is represented by dashes and RIC by solid lines. Colors correspond with configuration. The correlation for RIC used is for dose rates between 10^4 rad/s and 5 x 10^7 rad/s from Table 5.

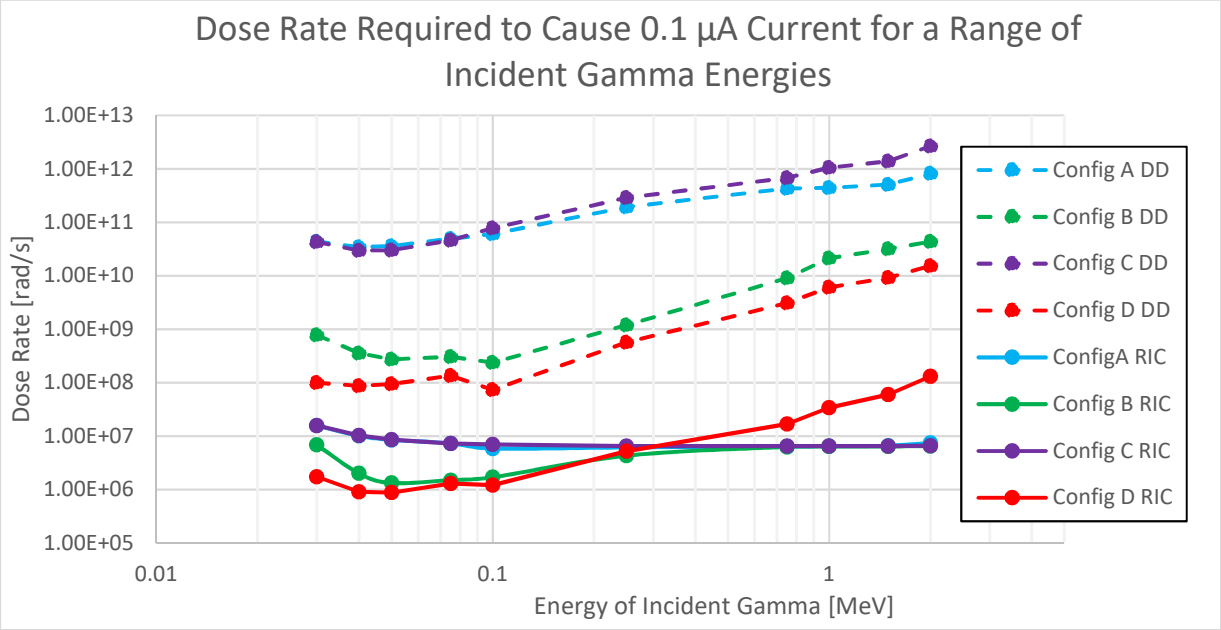

Figure 45- Combined plot of direct drive and RIC effects for all four device configurations considered. The y-axis is the dose rate required to cause a 0.1 µA current for a given energy. All simulations were run with monodirectional and monoenergetic gammas in CEPXS. Direct drive is represented by dashes and RIC by solid lines. Colors correspond with configuration.

RIC varies with energy due solely to $\frac{\dot{D}_{Si\ \ 2}}{\dot{D}_{Surface}}$ in Equation 21, where $\dot{D}_{Surface}$ represents the surface dose kerma of the device (the standard convention in quantifying radiation effects in electronics is to use kerma at surface for incoming dose rate). Figure 46 is a plot of $\frac{\dot{D}_{Si\ \ 2}}{\dot{D}_{Surface}}$ vs energy for the four configurations.

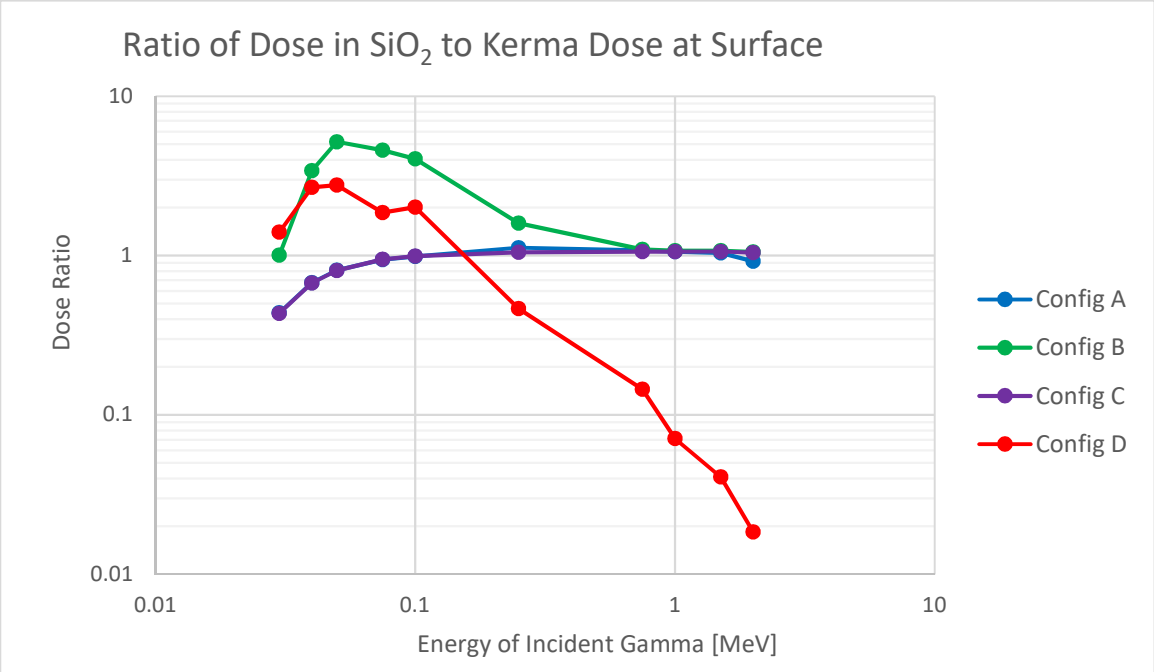

Figure 46- This Figure shows how dose in the SiO_2 layer compares with surface kerma. Surface kerma is generally used to indicate source strength in radiation effects on electronics.

Two major processes govern the behavior for Figure 46. Below 50 keV, self-attenuation of gamma rays by the VacFED results in a decrease of the dose ratio. Material differences govern the behavior above 50 keV. Configuration A has no bondpads and the attenuation coefficients of its materials are similar, resulting in the dose ratio approaching approximately unity. Configuration B has gold bondpads, which have a high attenuation coefficient at energies dominated by the photoelectric effect. The ranges of photoelectrons produced are within the distance to the SiO_2 layer, causing a large deposition of dose from electrons in SiO_2. As source-particle energies increase towards Compton-scattering dominant interactions, the attenuation cross sections of materials begin to converge and the dose ratio approaches unity. Configuration C has aluminum bondpads and behaves almost identically as

Configuration A because aluminum has a low atomic number and similar attenuation properties to the other materials in the VacFED.

The dose ratio for Configuration D decreases significantly below unity at energies above 0.1 MeV. This effect is due to the fact that Configuration D does not have equilibrators. Incident dose is measured in kerma at the surface. Kerma is a measure of the amount of energy that is transferred from photons to electrons. In Configuration D, most of the energy transferred to electrons is not absorbed in the device because the electron ranges are greater than the geometric boundaries of the device. In Configurations A-C, these exiting electrons are counteracted by an approximately equal number of incoming electrons produced in the equilibrators.

3.3.3 RIC MCNP Verification

Since RIC is dependent on the local dose in the SiO_2 layer, differences in transport methods could lead to a different predicted RIC current. Therefore, $\frac{\dot{D}_{SiO_2}}{\dot{D}_{Surfa}}$ is calculated using MCNP6 and compared to CEPXS for the 0.1 MeV case. The 0.1 MeV case is chosen because $\frac{\dot{D}_{SiO_2}}{\dot{D}_{Surface}}$ varies significantly from unity. Both 1-dimensional and 3-dimensional representations (reference Figures 38 and 41) were simulated in MCNP. The results are shown in Table 12. The relatively agreement in (less than 26% difference) between MCNP and CEPXS results provide validation to using 1-dimensional CEPXS calculations for RIC response.

Table 12- Comparison of ratio of dose in SiO_2 to the surface of the package for both MCNP and CEPXS for 0.1 MeV incident gammas. Dose ratio is proportional to RIC response. MCNP and CEPXS results differ at low energies due to differences in dose calculations due to electrons. Standard error reported in parentheses for all MCNP results.

	0.1 MeV				
Configuration	**$\frac{\dot{D}_{SiO_2}}{\dot{D}_{Surface}}$ from MCNP 1D**	**$\frac{\dot{D}_{SiO_2}}{\dot{D}_{Surface}}$ from MCNP 3D**	**$\frac{\dot{D}_{SiO_2}}{\dot{D}_{Surface}}$ from CEPXS**	**MCNP 1D % Difference from CEPXS**	**MCNP 3D % Difference from CEPXS**
A	1.03 (0.00)	1.00 (0.05)	0.99	4%	1%
B	4.00 (0.01)	3.36 (0.02)	4.05	1%	17%
C	0.99 (0.02)	0.93 (0.05)	0.99	0%	7%
D	1.78 (0.01)	1.50 (0.09)	2.02	13%	26%

4 Discussion and Future Work

This section proposes conservative limits for operation of VacFEDs in high dose rate radiation environments. It discusses the applicability of these results to sources of radiation other than photons and how to design VacFEDs to minimize radiation response. The final subsection discusses suggestions for future work including RIC coefficient research for insulating materials and long-term reactor testing of VacFEDs.

4.1 VacFED Radiation Tolerance

The ability of a VacFED diode to operate in a radiation environment was explored with a dose-rate induced noise current as the primary effect. An upper bound on radiation tolerance can be estimated based on a number of critical assumptions, including the current baseline design layout and materials and the best available material response parameters provided by the literature. A radiation tolerance level is proposed based on the findings of the previous section. Table 13 presents conservative estimates for gamma-dose rates at which VacFEDs can be operated in a continuous high dose rate environment with radiation-induced noise currents of 0.5 µA, 0.1 µA, and 0.01 µA respectively. These estimates are based on the Configuration A defined earlier and shown in Figures 28 and 29 using CEPXS with source gamma energy at 0.1 MeV.

Table 13- Proposed Radiation tolerance for operation of Configuration A VacFED.

Noise Current Mechanism	**Dose Rate [rad/s] to Cause 0.5 µA Noise Current**	**Dose Rate [rad/s] to Cause 0.1 µA Noise Current**	**Dose Rate [rad/s] to Cause 0.01 µA Noise Current**
RIC	3×10^{7}	6×10^{6}	6×10^{5}
Direct Drive from Gamma Dose	3×10^{11}	6×10^{10}	6×10^{9}

The dose rate tolerance estimates are a conservative lower bound for a number of reasons. These are derived from the CEPXS, a 1-dimensional transport model, which consistently reported greater RIC response than MCNP in both 1-dimensional and 3-dimensional configurations. Additionally, these

estimates are based on the gamma energy, 0.1 MeV, which creates the largest overall combined RIC and direct drive effect across the incident gamma energy range considered.

4.2 Radiation from Other Sources:

This thesis investigated gamma (photon) as an ionizing radiation source. Other ionizing sources of radiation will have similar effects and should be investigated further. Charged particles and heavy ions will also contribute to both direct drive and RIC current. Charged particles interactions liberate electrons when slowing down in matter, and thus contribute to direct drive. Monte Carlo codes capable of charged particle and electron coupled transport could be used to estimate RIC and direct drive response.

RIC is entirely dependent on local dose imparted to the oxide layer and is largely independent of the type of ionizing radiation [24]. For example, a neutron source depositing 100 rad(Si) in an insulator would create approximately the same change in conductivity as a 100 rad(Si) gamma source [24]. Therefore, if the dose of incoming particles of any type is known, RIC can be calculated in the same manner as gamma rays. On the contrary, direct drive cannot be determined simply from knowing the ionizing dose because different particles have their own electron yield according to their cross section or stopping power.

Neutron displacement damage and transmutation is another effect not explored in this paper and is a concern in environments with high neutron flux, such as a fission or fusion reactors. The cathode tip's emission properties are highly sensitive to small changes in the crystal structure and doping. This, in combination with its relatively small size, suggest it may be prone to displacement effects, although the probability of interaction would be small. Future research would need to be conducted to determine if this is a significant concern. For example, a VacFED diode's current–voltage (I-V) characteristic curve could be compared before and after long-term exposure to neutrons in a research reactor.

4.3 VacFED Hardening Concepts

This section focuses on general concepts for designing VacFEDs for increased radiation hardness to radiation induced noise current in high dose rate environments. The first subsection discusses hardening concepts for direct drive. The second subsection discusses hardening concepts for RIC.

4.3.1 Direct Drive Current

Hardening to direct drive-induced noise current requires minimizing the magnitude of the net deposition of electrons in the conductive layers, particularly the anode layer. Direct drive occurs due to liberation, transport, and deposition of electrons from radiation ionization interactions. Reducing the imbalance of liberated electrons reduces direct drive current in the conductive layers. In order to reduce electron production, use of high-Z and high density materials should be minimized in close proximity to the conducting layers and anode in particular. If these materials are necessary in surrounding circuitry, a sufficiently thick layer of low-Z material could be inserted to shield undesired liberated electrons from entering the anode.

Additionally, direct drive response will also be reduced through minimization of anode volume since direct drive current is directly proportional to anode volume. A larger anode volume will result in greater attenuation of incident radiation and the production of more gammas. Additionally, a larger anode volume increases the probability of electrons stopping in the anode.

4.3.2 Radiation Induced Conductivity Current

Hardening to RIC-induced current can be accomplished through maximizing the baseline resistance of the insulating oxide layer, eliminating unnecessary parts of the insulating layer, reducing the dose to the oxide layer, and selecting lower response insulating materials.

The resistance of the oxide layer is proportional to the length of a material divided by the cross-sectional area of the material. Thus, reducing the area of insulating material and increasing the thickness along any path to the anode will reduce the impact of RIC.

$$R = \rho(\dot{D})\frac{l}{A} \tag{23}$$

RIC current can be reduced though manipulation of the oxide geometry by etching out the SiO_2 in the gap between cathode and anode. This would effectively halve the RIC response from the primary current pathway of concern, pathway 3 of Figure 42, and eliminate current pathway 2 entirely. This simple change along with thickening the SiO_2 layer from 2 µm to 10 µm reduces RIC by approximately an order of magnitude, as shown in Figure 47.

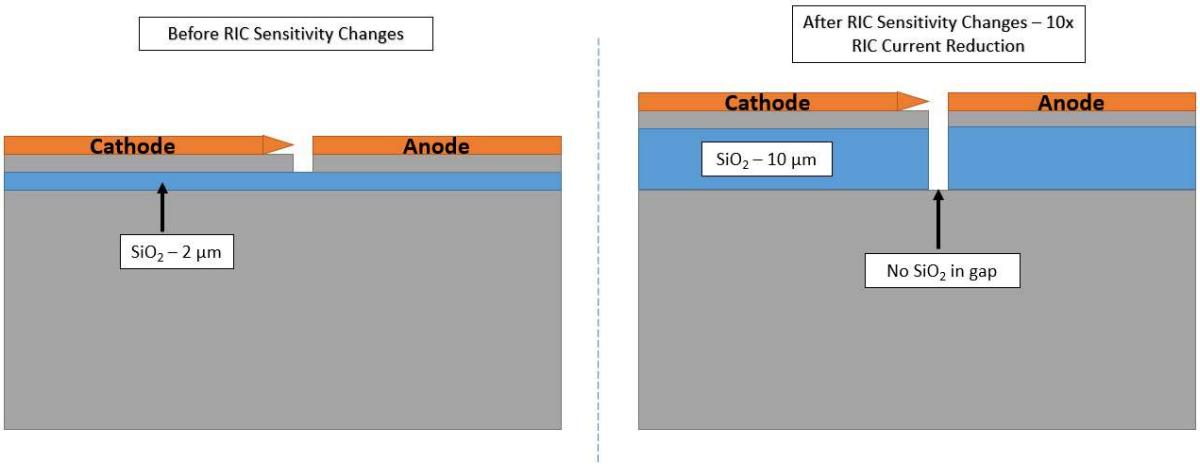

Figure 47- The left side of this Figure represents the Configuration A VacFED. The right represents the same VacFED with SiO_2 etched out between the cathode and anode to reduce cross-sectional area and with a greater SiO_2 thickness. RIC on the right-side diagram would be approximately a tenth of the left.

Minimizing the dose to the oxide layer can be accomplished by eliminating high-Z dense materials close to the SiO_2, which also reduces to direct drive response. High-Z layers should be minimized, especially when the source of radiation is low-energy x-rays or gamma rays. High-Z layers produce electrons through the photoelectric effect that can enhance localized dose in the oxide layer, increasing $\frac{\dot{D}_{SiO_2}}{\dot{D}_{Package}}$ from Equation 21.

Finally, materials with a lower RIC photoconductivity could be explored as insulators. This thesis focused on SiO_2 because it is ubiquitously used in semi-conductor and MEMS manufacturing. The conductivity of irradiated materials varies greatly with material [29]. Materials with lower RIC response could be considered when implementing VacFEDs in extreme radiation environments. RIC in various materials are shown in Figure 48 [29]. The lower theoretical bounds shown on the figure are proportional to the mass density of the insulating material divided by the square of the band gap energy [29]. Polymers such as polystyrene, polyisobutylene, and polyethylene terephthalate could offer increased resistance to RIC according to this figure.

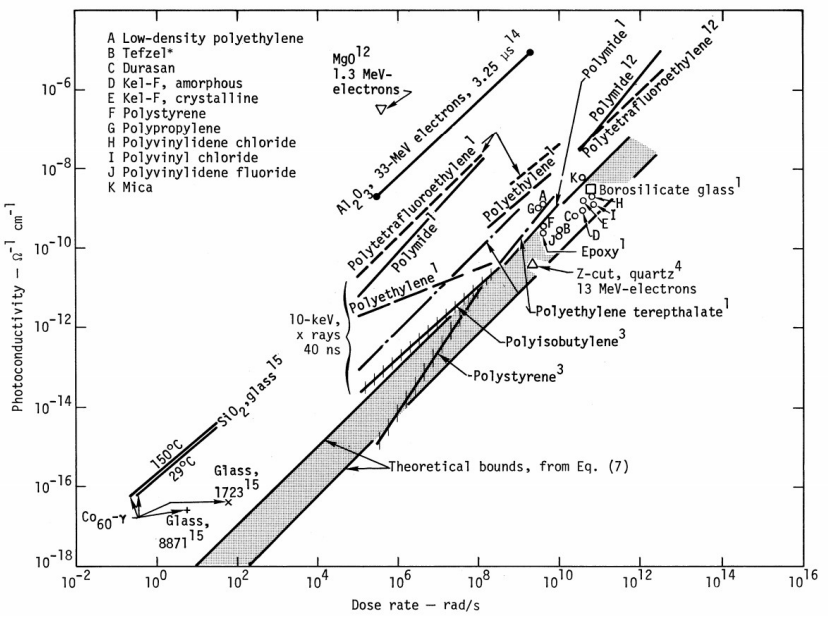

Figure 48- RIC in various materials based on pulsed data [29].

4.4 Suggestions for Future Work

To better predict radiation response of VacFEDs, experimentation is necessary. Research into RIC coefficient in persistent high dose rate exposure should be conducted for SiO_2 and other insulating materials of interest. Additionally, long-term reactor testing should be conducted to assess potential displacement effects from neutrons.

4.4.1 RIC Coefficient research

This thesis found that RIC is the dominant radiation effect in VacFEDs. The derived RIC currents made in this thesis are based on photoconductivity coefficients of previous RIC experiments from the literature [30] [21]. These coefficients were generated from experiments that do not match VacFED operational conditions nor materials. These experiments tested a different type of SiO_2, used limited dose rate ranges, used only pulsed radiation, and only tested high dose-rate RIC effects at room temperature. Therefore, the RIC coefficients are in need of experimental validation and exploration.

The SiO_2 used in VacFEDs and MEMS manufacturing in general is thermally grown native oxide. The RIC coefficients in this thesis were determined from fused SiO_2 glass. The sheet resistivity of a native grown

oxide is generally greater than that of fused glass since it contains fewer impurities [31]**.** Therefore, RIC coefficients need to be determined for native grown SiO_2 through experimentation.

Additionally, the experimental setup and geometry of the SiO_2 used is often quite different than the application in VacFEDs. The thickness of SiO_2 was 254 μm in the experiment used to determine RIC coefficients for ionizing doses above 10^4 rad(Si)/s. The RIC coefficients used in this paper are shown previously in Table 5. These coefficients are drawn from two different experiments, one at lower dose rates (0-10^2 rad(Si)/s) and one at much higher rates (10^4-10^{10} rad(Si)/s). In order to predict RIC response better and draw stronger conclusions on radiation effects on VacFEDs, RIC coefficients should be determined from SiO_2 thicknesses closer to that used in VacFEDs (about 2 μm) with a wide range of dose rates.

Furthermore, this paper uses RIC coefficients based primarily on room temperature tests. RIC correlations are dependent on temperature [24]. Data exists on the effect of temperature on RIC response in SiO_2, however these experiments all occur at only low dose rates where RIC would have minimal impact on a VacFED [32] [30]. One such experiment is shown in Figure 49. In this experiment, RIC is measured at four different temperatures with dose rates ranging from 0.3 rad(H_2O)/s to 10 rad(H_2O/s). In this range of dose rates, a 150 ℃ environment caused approximately 60% more conductivity than a 29 ℃ environment. In order to assess applicability for high temperature and high dose environments, such as a reactor (operate at temperatures of approximately 300 ℃), more experiments would need to be conducted.

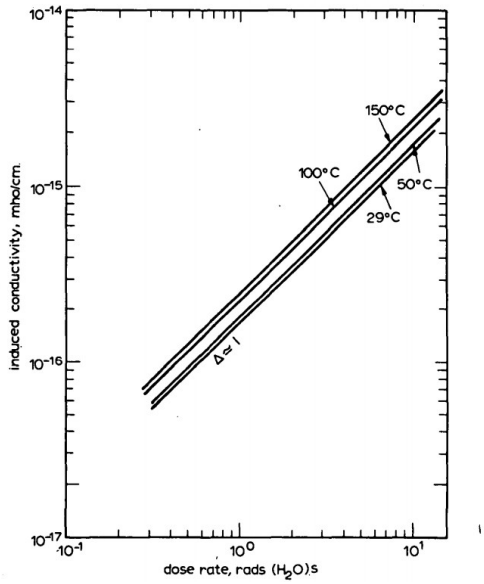

Figure 49- RIC in fused SiO_2 at different temperatures from [32]. The dose rates explored are much lower than those identified to cause concern in VacFEDs.

This thesis also used RIC coefficients from pulsed exposures and considered the former as a conservative upper-limit because space charge effects increase the likelihood of recombination of charge carriers, thus reducing RIC over time [21] [24]. In order to truly assess the viability of VacFEDs in continuous radiation environments, such as in a reactor environment, additional research should be conducted that measure the coefficient over continuous exposure. Additionally, electrical models should be studied to assess potential charge buildup in insulating layers at various dose rates.

4.4.1.1 Simple RIC Experiment

One simple experiment that should be carried out in order to more accurately assess RIC effects is shown in Figure 50. SiO_2 should be placed in a capacitor arrangement held at a voltage relevant to VacFED operation, such as 10 V. The thickness of SiO_2 should also be similar to the thickness in a VacFED. The cross-sectional area of the SiO_2 should be large enough to elicit a measurable RIC current. This can be determined from Equation (20) of section 3.3.1. Radiation from an x-ray source should be incident to the device and measured with a dosimeter at the surface. The change in current flow through the circuit as a function of incident radiation could then be collected from a continuous source and changes in resistivity could be calculated.

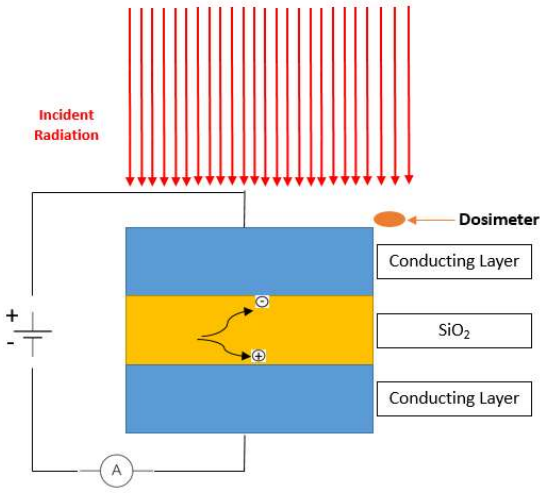

Figure 50- Simple diagram of experiment to determine RIC coefficients in a thin layer of SIO_2. Current through the circuit is measured with an ammeter and should be plotted versus incident dose determined by a dosimeter.

This simple experiment would serve multiple purposes. It would verify and update existing RIC data for SiO_2 in an experimental setup more closely resembling a VacFED. Use of an x-ray source would allow for measurement of RIC under continuous radiation. Tests for both pulsed and continuous x-ray sources should be run. Additionally, the temperature could be varied to assess temperature effects combined with dose rate on RIC. To test suitability in a PWR nuclear reactor core, the temperature should be increased up to a minimum of 300 ℃.

4.4.2 Long-Term Reactor Testing

Additionally, the effects of long term exposure to radiation in a reactor could be assessed. Device performance should be tested before and after a long time of reactor exposure. This would determine whether the device is sensitive to displacement damage, as well as transmutation effects. Live testing could also be conducted to assess ionization effects due to radiation other than gammas, however this testing may be difficult. Previous research has exposed VacFEDs to up to 4.4×10^{13} neutrons/cm^2 with no discernable effects on device performance (live-testing was not performed) [7]. However, this is not a large fluence considering nuclear reactors have fluences exceeding 10^{18} n/cm^2 per year at the reactor

vessel wall [33]. VacFEDs operating in reactor environments would likely need to last a fuel cycle at minimum (generally 18 months or greater) before they can be replaced.

5 Conclusion

The unique design of VacFEDs offer the potential to operate in radiation environments that would be considered impractical for semiconductors without a large amount of shielding and radiation-hardening techniques. This thesis found a dose rate of 6 x 10^6 rad(Si)/s at the surface of a VacFED diode is required to cause a 0.1 µA noise current in a device designed to operate at 1.0 µA. This finding suggests that VacFED technology has the capability to operate continuously in a modern pressurized water nuclear reactor core gamma ray environment, which has an approximate dose rate of 3 x 10^5 rad(Si)/s. Table 14 shows proposed limits for the device shown in Figure 51. This device was chosen for this thesis because it is a VacFED that can be realistically created with current technology with an operating current of approximately 1.0 µA.

Table 14- Proposed limits for operation of current state-of-the-art VacFED (Named Configuration A in this thesis) for three different levels of acceptable noise current.

Noise Current Mechanism	**Dose Rate [rad/s] to Cause 0.5 µA Noise Current**	**Dose Rate [rad/s] to Cause 0.1 µA Noise Current**	**Dose Rate [rad/s] to Cause 0.01 µA Noise Current**
RIC	3 x 10^7	6 x 10^6	6 x 10^5
Direct Drive from Gamma Dose	3 x 10^{11}	6 x 10^{10}	6 x 10^9

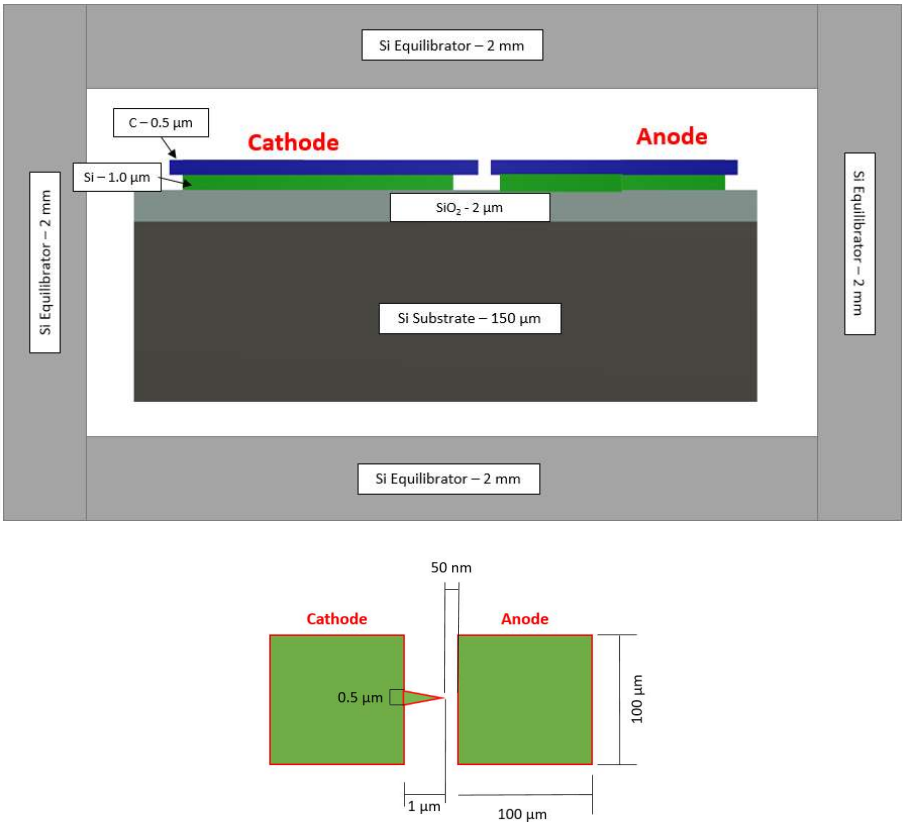

Figure 51- Model of Configuration A VacFED used to determine limits in Table 14 in two different planes.

The two effects from radiation explored in this thesis are direct drive and radiation induced conductivity (RIC). Direct drive is a net current of electrons in or out of the conductive layers of the VacFED device as a result of an imbalance in liberated electrons from ionizing radiation. RIC is the increased conductivity of an insulating material due to ionizing radiation dose rate. These effects were both explored using a 1-dimensional code discrete ordinates radiation transport code, CEPXS, and a 3-dimensional Monte Carlo radiation transport code, MCNP. The results of these two codes were used to propose the limits shown in Table 14. Additional configurations than that shown in Figure 51 were also tested with different incoming radiation energies. RIC current dominates over direct drive over all configurations as shown in Figure 52.

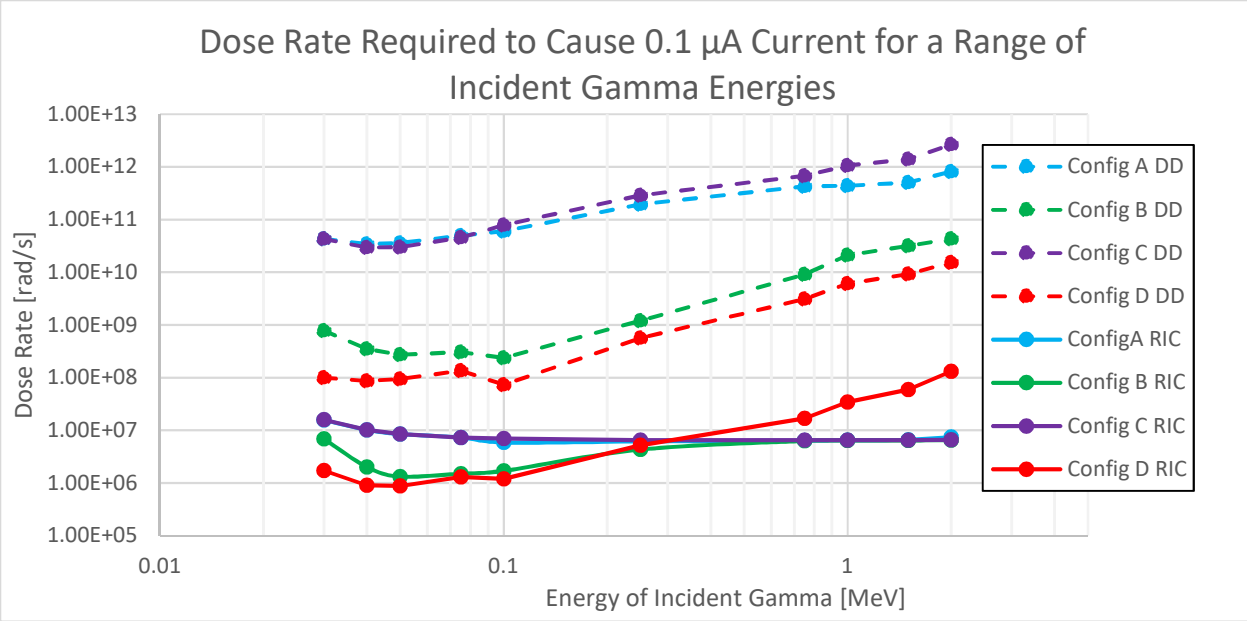

Figure 52- Combined plot of direct drive and RIC effects for all four device configurations considered. The y-axis is the dose rate required to cause a 0.1 µA current for a given energy. Direct drive is represented by dashes and RIC by solid lines. Colors correspond with configuration.

Previous speculation and results suggest vacuum field emission devices are relatively radiation insensitive [5] [6]. However, no significant research exists experimentally testing the live-performance of VacFEDs in high-radiation environments. This thesis found VacFEDs are able to sustain noise currents of less than 0.1 µA up to incident gamma ray doses of 6×10^6 rad(Si)/s. However, it attempted to model live performance with significant limitations that exist in the supporting data. There exists a lack of RIC response data for SiO_2 buried in oxide, high temperatures, or response to continuous dose. Neutron displacement effects are not assessed. Due to these limitations, this thesis can only offer rough conservative limits for operation of VacFEDs in high radiation environments. Experimental testing should be conducted to assess the actual effects of incident gamma dose and to assess the potential effects of displacement damage from neutrons.

6 References

[1] M. Gaillardin, M. Martinez, P. Paillet, F. Andrieu, S. Girard, M. Raine, C. Marcandella, O. Duhamel, N. Richard and O. Faynot, "Impact of SOI Substrate on the Radiation Response of UltraThin Transistors Down to the 20 nm Node," *IEEE Transactions on Nuclear Science,* vol. 60, no. 4, pp. 2583-2589, 2013.

[2] K. Label, "Proton Single Event Effects (SEE) Guideline," NASA Electronic Parts and Packaging (NEPP) Program, Washington, D.C., 2009.

[3] "Forward Biased p-n Junction Diode," Physics and Radio-Electronics, 2015. [Online]. [Accessed 19 July 2018].

[4] D. Makowski, "The Impact of Radiation on Electronic Devices with the Special Consideration of Neutron and Gamma Radiation Monitoring," Technical University of Lodz, Lodz, 2004.

[5] K. Subramanian, W. Kang, J. Davidson, N. Ghosh and K. Galloway, "A Review of Recent Results on Diamond Vacuum Lateral Field Emission Device Operation in Radiation Environments," *Microelectronic Engineering,* vol. 88, no. 9, pp. 2924-2929, 2011.

[6] A. Wisitsorat-at, "Micropatterned Diamond Vacuum Fiel Emission Devices," Vanderbilt University, Nashville, 2002.

[7] J. Davidson, W. P. S. K. Kange, A. Holmes-Siedle, R. Reed and K. Galloway, "Diamond Vacuum Electronic Device Behavior After High Neutron Fluence Exposure," *IEEE Transactions on Nuclear Science,* vol. 56, no. 4, pp. 2225-2229, 2009.

[8] W. P. Kang, J. L. Davidson, K. Subramanian, B. K. Choi and K. F. Galloway, "Nanodiamond Lateral VFEM Technology for Harsh Environments," *IEEE Transactions on Nuclear Science,* vol. 54, no. 4, pp. 1061-1065, 2007.

[9] J. Hubbell and S. Seltzer, "X-Ray Mass Attenuation Coefficients: NIST Standard Reference Database 126," National Institute of Standards and Technology, Gaithersburg, 2018.

[10] G. Famulari, "Production and evaluation of novel brachytherapy sources," McGill University, Montreal, 2016.

[11] F. Bubb, "Direction of Ejection of Photo-Electrons By Polarized X-Rays," *American Physical Society Physics Review,* vol. 23, pp. 137-144, 1924.

[12] MIT Open Courseware, *Interactions of Photons with Matter,* Cambridge: MIT Department of Nuclear Science and Engineering, 2004.

[13] L. Tlustos and E. Heijne, "Performance and limitations of high granularity single photon processing X-ray imaging detectors," 2005.

[14] P. Hough, "The Angular Distribution of Pair-Produced Electrons and Bremsstrahlung," *Phys. Rev,* vol. 74, no. 1, pp. 80-86, 1948.

[15] P. Sigmund, "Stopping of Swift Point Charge I: Bohr and Bethe Theory," in *Particle Penetration and Radiation Effects*, Heidelberg, Springer, 2006, pp. 109-139.

[16] "ESTAR: Stopping Powers and Ranges for Electrons," National Institute of standards and Technology, Gaithersburg.

[17] P. Miraglia, *Technical Explanation of the Challenge of Collecting Low energy Secondary Electrons,* Cambridge, 2017.

[18] L. M. J. V. G. Lorence, "User's Guide to CEPXS/ONEDANT," Sandia National Laboratories, Albuquerque, 1989.

[19] Los Alamos National Laboratory, "MCNP6.1/MCNP5/MCNPX Manual," Los Alamos National Laboratory, Los Alamos, 2013.

[20] S. Face, c. Eklund and T. Stringer, "Measurement of radiation induced conductivity for hardened cable dielectric materials at high fluence," *IEEE Transactions on Nuclear Science,* vol. 6, pp. 4450-4456, 1983.

[21] M. H. f. Mclain, T. Zarick, H. Hjalmarson, J. Gleason, K. McDonald and T. Sheridan, "Effects of High Dose Rate Ionizing Radiation on Fused Silica and Sapphire Films," *IEEE Transactions on Nuclear Science,* vol. 60, no. 6, pp. 4116-4121, 2013.

[22] J. Dennison, "Radiation Induced Conductivity and Cathodoluminescence of Disordered SiO2," Utah State University, Logan, 2013.

[23] J. Gillespie, "Measurement of The Temperature Dependence of Radiation Induced Conductivity in Polymeric Dielectrics," Utah State University, Logan, 2013.

[24] V. J. Van Lint, J. Harrity and T. Flanagan, "Scaling Laws for Ionization Effects in Insulators," *IEEE Transactions on Nuclear Science,* vol. 15, no. 6, pp. 194-204, 1968.

[25] S. Zinkle and E. Hodgson, "Radiation-induced changes in the physical properties of ceramic materials," *Journal of Nuclear Materials,* vol. 191, pp. 58-66, 1992.

[26] J. Hunn, R. Stoller and S. Zinkle, "In-situ measurement of radiation-induced conductivity of thin film ceramics," *Journal of Nuclear Materials,* vol. 219, pp. 169-175, 1995.

[27] Draper, "Nitrogen-doped nanocrystalline diamond growth experiments," Cambridge, 2018.

[28] T. Kamins, Polycrystalline Silicon for Integrated Circuits and Displays 2nd Edition, New York: Springer US, 1998.

[29] T. J. Ahrens and F. Wooten, "Electrical Conductivity Induced in Insulators by Pulsed Radiation," *IEEE Transactions on Nuclear Science,* vol. 23, no. 3, pp. 1268-1272, 1976.

[30] J. Dennison, J. Corbridge Gillespie, J. Hodges, R. C. Hoffman, J. Abott, S. Hart and A. W. Hunt, "Temperature Dependence of Radiation Induced Conductivity in Insulators," *American Institute of Physics Conference Proceedings Series,* vol. 1099, pp. 203-208, 2009.

[31] J. Plummer, M. Deal and P. Griffin, Silicon VLSI Technology, Pearson, 2000.

[32] V. E. Culler and H. E. Rexford, "Gamma-Radiation-Induced Conductivity in Glasses," in *Conference on Electrical Insulation*, 1961.

[33] Areva, "KCB RPV Safet Assessment Assuming 60 Years of Operation," Areva, Erlangen, 2010.

[34] a. Nero, "A Guidebook to Nuclear Reactors," Lawrence Berkeley Laboratory, Berkely, 1976.

[35] International Atomic Energy Agency, "Determination of Absorbed Dose in Reactors," IAEA, Vienna, 1971.

[36] J. D. Spear, "Shot noise in x-ray measurements with p-i-n diodes," *Review of Scientific Instruments,* vol. 76, no. 7, 2005.

[37] K. Subramanian, W. Kang, J. Davidson, N. Ghosh and K. Galloway, "A review of recent results on diamond vacuum lateral field emission device operation in radiation environments," *Microelectronic Engineering,* vol. 88, no. 9, pp. 2924-2929, 2011.

[38] K. LaBel, "Radiaition effects on Electronics 101: Simple Concepts and New Challenges," NASA, 2004.

Appendix A - Additional 3-Dimensional Modelling of Configuration A Device with Monodirectional Source Gammas:

Three additional scenarios are included in this appendix to assess the effect of changing the direction of source gammas incident a VacFED in Configuration A. In Scenario A, gammas are incident on a 3-dimensional representation of the VacFED diode from both directions, parallel to the z-axis. Scenario A tests whether the addition of a small tip causes a significant imbalance in charge deposition. In Scenario B, gammas are incident parallel to the x-axis from both directions. This also tests whether the addition of a small tip causes a significant imbalance in charge deposition, but with different source geometry. In Scenario C, gammas are incident only on the conductive layers parallel to the x-axis in only one direction. Scenario C is included because a monodirectional gamma source in the direction of cathode to anode should create a larger imbalance of charge deposition between the cathode and anode due to photoelectric emission angle and Compton scattering angle probabilities. If no significant difference is found between cathode and anode charge deposition in Scenario C, then it would suggest the inclusion of a tip does not significantly affect direct drive current. Figure 53 shows the three scenarios. The top down view for each scenario is shown in Figure 29.

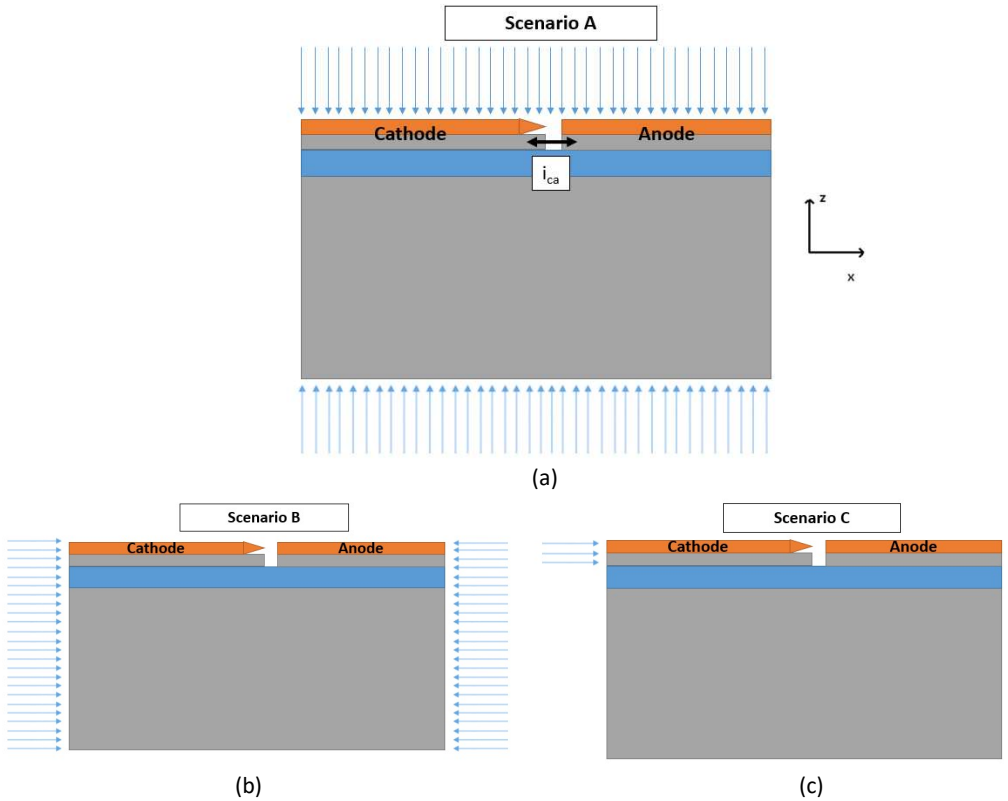

Figure 53- 3-dimensional models tested. In (a) gammas are parallel to the z-axis from both directions. i_{ca} represents a current imbalance between the cathode and anode. Quantifying the magnitude of this difference is the primary motivation for these three scenarios. In (b), source gammas are parallel to the x-axis from both directions. In (c), gammas are only presented in one direction and incident the conductive layer of the device. The top-down view is shown in Figure 29.

The number of electrons in the conductive layer (the summation of the carbon and thin silicon layers) are tallied for each scenario in both the cathode and anode. These tallies, along with their differences in Table 15.

Table 15- This table shows the differences in electron deposition between the cathode and anode conductive layers. These differences are insignificant, supporting the utility of a 1-dimensional model in the x-z plane. Relative standard error for MCNP is reported in parentheses.

Scenario	Cathode Electron Deposition per Source Particle in Conductive Layers (e^-/γ)	Anode Electron Deposition per Source Particle in Conductive Layers (e^-/γ)	% Difference between Cathode and Anode
A	1.192×10^{-5} (0.013)	1.172×10^{-5} (0.013)	1.7%
B	1.391×10^{-5} (0.009)	1.407×10^{-7} (0.009)	0.9%
C	2.135×10^{-5} (0.002)	2.111×10^{-5} (0.002)	1.1%

The difference between the cathode and anode electron deposition is approximately 2 orders of magnitude less than the number of electrons deposited in each scenario. This small discrepancy would not cause a significant direct drive effect. This validates the utility of 1-dimensional simulations in the x-z plane, as performed in all CEPXS 1-dimensional simulations in this thesis, because the geometric imbalance between the cathode and the anode does not appear to contribute significantly to the direct drive current. This could change if cathode tip geometries are modified such that they are of comparable size to the anode. However, this is not seen in modern VacFED designs. The importance of any cathode-anode imbalance is diminished considering the RIC current is generally orders of magnitude larger than the direct drive current.

Appendix B - Estimation of Gamma Dose Rate in a Nuclear Reactor

The dose due to gamma rays in a PWR can be estimated knowing a few approximate reactor parameters:

Reactor Power Density (P/V): 98 [W/cm^3] [34]

Average Gamma Energy Absorbed per Fission (E_γ): 14.7 [MeV] [35]

Average total Energy Absorbed in Reactor (E_{tot}): 199 [MeV] [35]

Density of Silicon (ρ): 2.33 [g/cm^3]

The Gamma power density is calculated as:

$$\frac{P_\gamma}{V} = \frac{E_\gamma}{E_{tot}} * \frac{P}{V} = 7.2 \left[\frac{W}{cm^3}\right] \tag{24}$$

Dose rate, $\dot{D}$ is defined as power, P, divided by mass, m:

$$\dot{D} = \frac{P}{m} = \frac{P_\gamma}{V} * \frac{1}{\rho} = 7.2 \left[\frac{W}{cm^3}\right] * \frac{1}{2.33 \left[\frac{g}{cm^3}\right]} * \frac{1 \left[\frac{rad}{s}\right]}{1\ x\ 10^{-5} \left[\frac{W}{g}\right]} = 3.1\ x\ 10^5 \left[\frac{rad}{s}\right] \tag{25}$$

Therefore, the dose rate in a reactor due to gamma rays can be estimated as approximately 3.1 x 10^5 rad/s.